Iron is neurotoxic in retinal detachment and transferrin confers neuroprotection

Alejandra Daruich, Quentin Le Rouzic, Laurent Jonet, Marie-Christine Naud, Laura Kowalczuk, Jean-Antoine Pournaras, Jeffrey H Boatright, Aurélien Thomas, Natacha Turck, Alexandre Moulin, et al.

Title

Iron is neurotoxic in retinal detachment and transferrin confers neuroprotection

Short title: Iron in retinal detachment - transferrin treatment

Authors

Alejandra Daruich[1,2,3], Quentin Le Rouzic[1], Laurent Jonet[1], Marie-Christine Naud[1], Laura Kowalczuk[2], Jean-Antoine Pournaras[2], Jeffrey H. Boatright[4,5], Aurélien Thomas[6,7], Natacha Turck[7,8], Alexandre Moulin[2], Francine Behar-Cohen*[1,7,9], Emilie Picard[1]

Affiliations

1. INSERM, UMRS1138, Team 17, From physiopathology of ocular diseases to clinical development, Université Sorbonne Paris Cité, Centre de Recherche des Cordeliers, 15 rue de l'Ecole de Médecine, 75006 Paris, France
2. Department of ophthalmology, University of Lausanne, Jules-Gonin Eye Hospital, Fondation Asile des Aveugles, Lausanne, Switzerland
3. Ophthalmology Department, Necker-Enfants Malades University Hospital, AP-HP, Paris, France.
4. Department of Ophthalmology, School of Medicine, Emory University, Atlanta, GA, United States
5. Center of Excellence, Atlanta Veterans Administration Medical Center, Decatur, GA, United States
6. Geneva University Hospitals; Unit of Toxicology, CURML; Geneva, Switzerland
7. Faculty of Biology and Medicine, University of Lausanne, Rue du Bugnon 21, 1011 Lausanne, Switzerland
8. Geneva University, Department of Human Protein Science; Geneva, Suisse Ophtalmopole,

9. Cochin Hospital, AP-HP, Assistance Publique Hôpitaux de Paris, 24 rue du Faubourg Saint-Jacques, 75014 Paris, France

*Corresponding author: Francine Behar-Cohen; francine.behar@gmail.com; INSERM, Centre de Recherche des Cordeliers, 15 rue de l'école de médecine, 75006 Paris, France

Teaser (150words)

Ocular fluids from patients with retinal detachment show iron accumulation and transferrin can be used as a therapeutic adjuvant.

Abstract

In retinal detachment (RD), photoreceptor death and permanent vision loss is caused by neurosensory retina separating from the retinal pigment epithelium because of subretinal fluid (SRF), and successful surgical reattachment is not predictive of total visual recovery. As retinal iron overload exacerbates cell death in retinal diseases, we assessed iron as a predictive marker and therapeutic target for RD. In the vitreous and SRF from RD patients, we measured increased iron and transferrin (TF) saturation that is correlated with poor visual recovery. In *ex vivo* and *in vivo* RD models, iron induces immediate necrosis and delayed apoptosis. We demonstrate that TF decreases both apoptosis and necroptosis induced by RD and using RNA sequencing, pathways mediating the neuroprotective effects of TF are identified. Since toxic iron accumulates in RD, we propose TF supplementation as an adjunctive therapy to surgery for improving the visual outcomes of RD patients.

MAIN TEXT

Introduction

Retinal detachment is an ocular emergency, as separation of the neuroretina from the underlying retinal pigment epithelium (RPE) (Fig. **1A**) disturbs photoreceptor (PR) metabolism causing PR death and subsequent vision loss (*1*). In rhegmatogenous retinal detachment (RRD), a retinal tear (arrowhead, **Fig. 1A**) induces subretinal fluid (SRF) accumulation in a space formed between the neuroretina and the RPE. The incidence of adult RRD varies between 10 to 55 per 100,000 individuals/year, with higher occurrence in patients who also have myopia or pseudophakia (*2*). This incidence will likely rise with myopia increasing worldwide (*3*). Intraocular surgery is commonly used to repair RRD but must be realized rapidly after detachment, as the duration of macular detachment is one of the major visual prognosis factors (*4*). The principles of surgery are based on retinal breaks closure (i.e., by laser therapy or cryotherapy) and internal or external temporary tamponade to maintain the retina attached during wound healing. When the procedure is performed internally, vitreous is removed and SRF is eventually extracted. Despite tremendous progress made in surgical techniques and the high repair rate, 60% of patients with RRD involving the macula (macula-OFF RD, 50% of the cases) recover less than 20/40 vision (*4*), and have poor vision-related quality of life (*5*). Improving vision after retinal detachment surgery is thus a critical therapeutic challenge.

Experimental models of retinal detachment (RD) correlate well with human pathology, making them appropriate to study mechanisms and pharmacotherapeutic strategies. First changes are observed at the RPE/PR interface (*6*), followed by PR cell death that peaks at 2-3 days through apoptosis, necrosis and autophagic cell death mechanisms (*1*). Interestingly, caspase inhibitors do not prevent cell death in RRD models , but rather promote receptor interacting protein kinase (RIP)-kinase dependent necrosis, referred to as necroptosis (*7*). Subsequent inflammatory reactions, including macrophage/microglial activation contribute to a neurotoxic environment and to subsequent gliosis (*8*). Factors initiating cell death during RD remain undetermined, and the identification of a common target of the different death mechanisms is mandatory for developing an effective neuroprotective strategy for RD.

Iron is an important biological component for catalyzing enzymatic reactions. But when it is poorly liganded, iron generates reactive oxygen species and damaging cellular components (*9*). Iron-mediated retinal cell death has been suspected to occur in various forms of retinal degeneration (*10*), including age-related macular degeneration (*10*), the leading cause of blindness in developed countries, but no correlation between iron and visual function was possible and the iron sequestration capacity in human ocular fluids has never been evaluated in relation to retinal diseases. The control of ocular iron homeostasis is tightly controlled by retinal cell proteins, and the iron transporter, transferrin (TF), is one major protein found in the vitreous. We previously showed that the sequestration of two ferric iron ions by TF (*11*) prevents the formation of free radical-mediated stress and glial retinal cell death in culture. Our previous studies also showed, in various animal models, that treatment with TF exerted retinal neuroprotective effects through the reduction of apoptosis, inflammation and oxidative stress (*12*, *13*). However, the molecular mediators and pathways involved in the protective effects of TF have never been investigated in depth.

In our study, we evaluated for the first time the iron and transferrin status in ocular fluids from RRD patients and correlated those parameters to visual acuity recovery and duration of RRD. Retinal explants are a common tool used for RD studies, recapitulating pathological processes found in the detached retina (*14*). Thus, we established an *ex vivo* model of RRD by placing rodent retinas in iron-overload culture conditions and investigated whether TF protects the retina by evaluating apoptosis, necroptosis, and oxidative stress cell markers. Transgenic mice expressing human TF in the retina were used to observe TF neuroprotective efficiency in an experimentally induced RD model (*15*), and using an RNA sequencing approach to explored the pathways implied in these effects. Intravitreal injection of TF in rats following experimental RD was used to determine the potential of TF as an adjuvant for RD surgery.

Results

In ocular fluids from patients with RRD, iron increases with detachment duration and correlates with poor visual recovery

Total iron, TF, TF iron-binding capacity (TIBC), and percentage of iron saturation (TSAT) were evaluated in undiluted vitreous and SRF collected from patients with RRD (age: 64.3 years; SD: 9.6; 11

females, 24 males, n=35), and from control patients (age: 70.2 years; SD: 9.5, 5 females, 4 males, n=9). In the vitreous, the level of iron was significantly higher in patients with RRD as compared to control subjects without retinal detachment (143.1 ng/ml ±14.4 vs 81.7 ng/ml ±16.8, p=0.046) (**Fig. 1B**). The TIBC values did not differ in eyes with or without RRD (4.5 ±0.7 and 4.3 ±0.6 µmol/L of TF, p>0.5) but TSAT increased from 22.8% ±3.8 in control eyes to 89.91% ±11.4 in eyes with RRD, reaching almost complete saturation (p=0.006) (**Fig. 1C and D**). In the SRF, the high rate of TF saturation (53.5% ±12.6) (**Fig. 1E**) also reflected iron overload. Higher levels of iron in the SRF were associated with longer duration of detachment (**Fig. 1E**, left graph, p=0.038) and correlated with lower visual recovery one month after surgery (**Fig. 1E**, right graph, p=0.047). Though the data are correlative, these results suggest that iron toxicity could contribute to the functional outcome in RRD.

Iron deposits, evaluated in post-mortem ocular tissues sections of RD, were found in the remaining PR layer, inside cells in the subretinal space very likely to be **inflammatory cells** (arrows) and in RPE (**Fig. 1F**) using Perl's staining. Inductively coupled plasma mass spectrometer (ICP-MS) analysis confirmed elevated iron content throughout the retina sections (**Fig. 1G**, green), with higher concentrations in focal areas (red, arrowheads). These observations suggest that iron could mediate, at least partially, PR damage during RRD.

Iron induces photoreceptors death in rat retinal explants *ex vivo*

To evaluate iron neurotoxicity, rat neural retina explants were cultured in low-serum medium and PR cells were immediately exposed to iron at a range of concentrations similar to those measured in SRF from RRD patients. After 2 days of exposure to 1 mM $FeSO_4$ (fig. S1A), no increase in caspase-dependent apoptosis was observed (caspase 3 activation and TUNEL positive cells were similar in control and iron conditions) (fig. S1B and C). Caspase-independent apoptosis and autophagy evaluated by the expression of AIF, LEI/L-DNase II, and LC3B I/II proteins were also not activated by iron exposure (data not shown). However, lactate dehydrogenase (LDH) release, an early marker of necrosis, was concentration-dependently increased as early as one-day post-iron overload exposure (fig. S1D). After 2 days of iron overload, necroptosis was confirmed with an increase of RIP kinase protein expression and staining of PR nuclei with propidium iodide (fig. S1E and F). The two days of iron

exposure leads to the loss of both rods and cones PR, as shown by the decreased rhodopsin protein level with increasing concentration of $FeSO_4$, (**Fig. 2B**) and nearly no arrestin- positive cones remaining after 1 mM $FeSO_4$ exposure (**Fig. 2C**, arrows). After iron overload, progressive histologic damage appeared over time, leading to complete retinal layer disorganization and shortening of the residual PR segments (**Fig. 2D**). While iron staining was not observed in the retina during iron exposure (data not shown), 7 days after iron removal, iron diffusely stained the retinal explants, particularly in the remaining PR segments, and was concentrated in **inflammatory cells type** (brown, arrows) as observed in human retinal detachment sections (**Fig. 2E**). The direct contact of iron with PR led to immediate necroptosis that increased with higher iron concentrations and with longer iron exposure times.

Transferrin protects against iron-induced toxicity in *ex vivo* mouse and rat retinal explants

In transgenic (TG) mice expressing human TF (hTF) in retinal cells (*11*), hTF levels increased in the medium with the duration of retinal explants culture (fig. S2 A to C). TG-derived explants exhibited fewer signs of degeneration and oxidative stress in low-serum medium compared with WT explants. After 6 days of culture, retinal glial Müller cells activation, identified by glial fibrillary acidic protein (GFAP) distribution (*16*) (fig. S2D, arrow), and markers of oxidative stress (8-hydroxyguanosine [8-HGN] and 4-hydroxynonenal [4-HNE]) (fig. S2 E and F) were reduced in retinal explants from TG mice, compared with those from WT mice.

Subsequently, we investigated whether TF was protective against iron overload combined with RD. Iron overload conditions were applied to TG and WT retinal explants (**Fig. 3A**). LDH release, evaluated after one day, was reduced by 24.4% in retinal explants from TG mice as compared with explants from WT mice ($p=0.03$) (**Fig. 3B**). After 6 days of iron exposure, the number of cones was 55.5% higher and the outer segment lengths were 58.2% longer in retinas from TG mice as compared with WT ($p<0.0001$ for both) (**Fig. 3C**). In addition, reduced Müller glial cell activation and oxidative stress markers (**fig. S3 A to C**) were observed in retinal explants from TG mice. The expression of hTF in TG mice retinas reduced iron accumulation as indicated by a reduction in ferritin light-chain (LFt) staining (**Fig. 3D**) (*12*). The TG mouse retinas were thus protected from iron-induced oxidative stress and necroptosis.

We then evaluated the effect of TF added to rat retinal explants after 2 days of iron exposure to more closely mimic the therapeutic time-course common in human RD treatment. After 2 days, iron was removed and exogenous hTF (50 mg/ml) was added in the medium (**Fig. 3E**). TF treatment rescued not only rod-specific protein (61.7% greater rhodopsin level (p=0.021) **(Fig. 3F)** and the lengths of rod outer segments (**Fig. 3G**, asterisk), but also cones (83.8% greater number of cones versus untreated (p=0.04)) (**Fig. 3G**, arrows). Two days after iron exposure, the RIP kinase protein level remained elevated, but the presence of the cleaved form of RIP kinase proteins (**Fig. 3H**) suggested an activation of caspase 8, leading to a delayed activation of apoptosis (*7*). Treatment with hTF significantly reduced the level of cleaved RIP kinase by 76.1% (**Fig. 3H**, p=0.028), increased the anti-apoptotic protein Bcl2 by 83.3% (**Fig. 3I**, p=0.028), and reduced the number of TUNEL positive cells (**Fig 3J**). As expected, LFt staining intensity was reduced (**Fig. 3K**), in parallel to the reduction of iron deposits in the retina. Exogenous hTF prevented the activation of resident macrophages/microglial cells (**fig. S4A**, CD68, arrowheads), and decreased Müller glial cell activation (**fig. S4B**, GFAP, arrows). The iron-induced oxidative stress markers 4-HNE and 8-HGN were also decreased with hTF treatment (**fig. S4 C and D**). Taken together, these results demonstrate that treatment with exogenous TF efficiently protects the retina from two types of iron-induced toxicity: direct and early necroptosis and delayed apoptosis that could result from secondary iron-related effects.

Transferrin rescues the detached mouse retina *in vivo*

We induced partial retinal detachment in mice and rats (around 50-70% and 30-50% of the retinal surface, respectively). After 7 days, the detached retina was thickened, the outer nuclear layer (ONL) was disorganized, PR nuclei were pyknotic and outer segments were absent, and RPE cells were enlarged in the detached area (**fig. S5**). Similar to human RD, iron accumulated in the detached rodent outer retinas (**fig. S6 A and B**) and in rat ocular fluids (52.54% increase in total iron levels after 14 days of detachment, p=0.042) (**fig. S6C**). In TG mice (**Fig. 4**), hTF protected the detached retina from edematous thickening (21.7% decrease in retinal thickness of the detached retina/non-detached retina; p=0.045, designated by brackets in Fig. **4A**, quantified in the left graph of Fig. **4B**), from ONL thinning (20.3% decrease; p=0.033, Fig. **4B**, right graph) and prevented PR outer segment shortening (50%

decrease; p=0.047, graph in Fig. **4C** and arrowheads in Fig. **4A** and **4C**). TG detached retinas had 311.3% more cones than WT (p=0.025; **Fig. 4D**). Activation of Müller glial cells, observed not only in the areas of detached retinas but also in attached regions of WT mice (data not shown), was significantly reduced in TG mouse retinas (**Fig. 4E**, arrows). Compared with WT retinas, hTF expressed in TG retinas decreased *caspase 8* mRNA expression by 48.9% (p=0.008), the level of the cleaved form of caspase 3 protein by 57.1% (p=0.03), and the number of TUNEL positive cells in the ONL of detached retinas by 56.3% (p=0.03), demonstrating the anti-apoptotic effect of TF in the mouse RD model (**Fig. 4F**). RIP kinase protein levels were reduced by 35.4% in the TG detached retina compared with the WT (p=0.03) (**Fig. 4G**) suggesting that hTF reduced both apoptotic and necrotic cell death in the mouse RD model.

Molecular signature of hTF overexpression in the mouse retinal detachment model

We performed a genome-wide analysis (RNA-Seq) of neural retinas from TG and WT mice 4 days after induction of retinal detachment. From a total of 412 genes differentially regulated between TG and WT mice (1.5 fold-change, $p \leq 0.05$), 149 were up-regulated and 263 were down-regulated. An extensive list is provided in **data File S1**. The 20 most up- and down-regulated genes are listed in table **S1**. Gene ontology (GO) (biological process, molecular function, cellular compartments categories) and reactome pathways enrichment analysis demonstrated significantly affected categories in genes down-regulated or up-regulated in TG mice as compared with WT (**Fig. 5**; see **data File S1** for details). We regrouped the significantly enriched pathways into 10 groups according to their biological functions: Retina homeostasis, Neurological process, Phagocytosis, Immune system, Remodeling of extracellular matrix (ECM), Mechanisms of cell death, Metabolism, DNA/RNA regulation, Intracellular signaling, and others, which comprise other biological functions such as cellular proliferation and differentiation (**Fig. 5**). The Retina homeostasis group was solely composed with the most significantly enriched GO term: "Photoreceptor cell maintenance" which included genes related to the connector cilium linking the inner segment to the outer segment and playing a major role in rhodopsin transport toward outer segments disks. Pathways relative to the Neurological process group were especially involved in the regulation of neuron development and cognition. The Phagocytosis group was composed of the most significant biological process according to the reactome analysis ("ER-phagosome pathway") that was also

represented in GO analysis associated with the "Receptor-mediated endocytosis" and the "Regulation of vesicle fusion" pathways. Interestingly, the GO molecular function analysis revealed that "binding" was the most significantly enriched term (16 of a total of 29 terms) (**data File S1**). Furthermore, of the top 20 of genes up- and down-regulated, half of these were associated with "protein binding" Molecular Function (GO term classification) (table **S1**). Pathways regrouped in the Immune system group were also highly represented in the two enrichment analyses, and genes included in those were mostly up-regulated. Pathways related to the Mechanism of cell death group were represented by two GO biological process terms involved in the regulation of apoptotic processes. In the 40 most significantly regulated genes, 12 were implied in cell death processes (table **S1**). The GO analysis of the cellular components showed 19 significant enrichments which can be regrouped in 3 equal cellular compartments: the nucleus, the cytoplasm, and membranes (**data File S1**), reflecting cross talk between the cell membrane and the nucleus.

Among the 412 genes differentially regulated between TG and WT mice, 2 genes have direct interactions with TF, *Tfrc* and *Igfbp3* (*17*). The insulin-like growth factor binding protein 3 (*Igfbp3)* transcript was significantly increased in TG mouse retina compared with WT 4 days after RD induction (fold-change: 3.27, p=0.086, table **S1**). In the normal retina, the IGFBP3 protein was localized in PR segments (arrowhead), in retinal capillaries and in the outer plexiform layer (arrow) (**fig. S7A**). Western blots analysis confirmed an increase of 46.7% of IGFBP3 protein level in the retinas of TG mice compared with WT mice 7 days after RD (p=0.028) (**fig. S7B**).

Local ocular injection of transferrin preserves detached rat retinas *in vivo*

In a therapeutic perspective trial, intra-vitreous injection of hTF (50 mg/ml) showed protective effects in a rat RD model (Fig. **6A**). The retinal thickness of the detached retina/non-detached retina (Fig. **6A**, brackets and Fig **6B**, upper graph) was 14.2% lower in TF-treated rats (p=0.003), whereas the ONL thickness was preserved (30.6% reduction, p=0.013, Fig. **6B**, middle graph), and immunostaining of rods and cones PRs (Fig. **6C**) revealed preserved morphology. There was a 37.6% reduction of outer segment length (arrowhead, Fig. **6B and C**) in BSS RD rats compared to TF-treated rats (p=0.004, Fig. **6B**, lower graph). Therapeutic TF thus reduced edema of the detached retina and preserved PR

morphology. Taken together, these results indicate that TF, even if administrated at the time of RD, can prevent further retinal alterations and cell death.

Discussion

Iron accumulation**-induced oxidative stress** has been observed in neurodegenerative and retinal diseases (*9*) and causes rapid PR death (*10*), but no correlation between intraocular iron and visual function has been demonstrated in a human disease. In our study, we show for the first time in human eyes increased iron levels and TF saturation in the vitreous and SRF fluid, reflecting the accumulation of free iron in ocular tissues **(RPE, PRs and inflammatory cells like)** upon retinal detachment. Our results confirmed previous analyses which demonstrate increased oxidative stress in vitreous from RRD patients (*18*).

Increased iron following retinal detachment could result from a combination of factors. In physiologic conditions, retinal iron entry is actively controlled through TF uptake by its receptor at the RPE basal membrane that forms the outer retinal barrier. After detachment, acute RPE alteration (*6*) may favor free iron entry. Similarly, a breakdown of the inner blood-retinal barrier in an animal model of type 2 macular telangiectasia, a rare human disease, led to iron accumulation in the retina and PR degeneration (*19*). However, iron accumulation was also shown in retinal dystrophies, especially in PRs, without obvious barrier breakdowns (*20*) suggesting that other mechanisms contribute to iron increases. **PRs and RPE have high iron content because it is a cofactor in phototransduction enzymes and have a major role in iron retinal homeostasis** (*20*). RPE cells, through the phagocytosis of shed outer segments, recycles iron and exports it from the retina (*20*). During RD, the loss of contact between PR and RPE leads to **intracellular iron accumulation**, a mechanism described in the RCS dystrophic rat, a genetic model of defective outer segment phagocytosis (*20*). PRs are extremely sensitive to iron excess, but the exact mechanisms of this toxicity have not been fully determined. We used organotypic retinal cultures to show that direct contact with iron causes rapid PR necrosis. Peroxidation by iron of polyunsaturated fatty acids (PUFAs) in the outer segments could be one necrotic mechanism (*21*). Furthermore, when iron has accumulated in the retina **explant** and after its removal **from medium**, apoptotic cell death **observed** could result from intracellular molecular iron-induced oxidation through the Fenton/Haber–

Weiss reaction cycle (DNA, RNA, lipids, proteins) (*9*), as suggested by DNA breaks (8-HGN) and lipid peroxidation (4-HNE) **(Fig. S4)**. Thus, labile iron exerts deleterious extracellular and delayed intracellular effects. The fact that vision recovery in patients with RRD was inversely correlated with ocular iron levels suggests that iron toxicity could be one of the mechanisms of PR loss over the time course of RRD.

The observation of fully saturated TF in ocular fluids and of intracellular iron accumulation in the retina both suggest that iron loading capacities are saturated. Therefore, the use of iron appears as a relevant therapeutic therapy. Chemical chelators (deferiprone, deferoxamine, or deferasirox) have already been evaluated in neurogenerative diseases after systemic administration (*22*)**. However, long-term iron chelation therapy, routinely used for instance in beta-thalassemia and chronic iron overload diseases impacts negatively patient's quality of life, and induced ocular toxicity, including cataracts, maculopathy, and optic neuritis** (*23*, *24*)**. Thus, the use of such chemical chelators in RD patients without systemic iron overload could be deleterious for the eye. Moreover, intraocular local administration of chemical iron chelators would require repeated intravitreal injections due to their short half-life** (*25*)**. Such local administration might cause excessive intracellular iron depletion due to high chelator to iron ratio.** Based on these finding, we proposed to use local ocular TF to neutralize iron toxicity. **We previously showed that TF is safe for ocular use even at high doses, prevents iron accumulation in RPE and PRs and that iron-loaded (holoTF) as well as iron-free TF egresses the retina through the TF receptor at RPE apical side** (*12*). **Using various models of retinal degeneration, we have previously showed that apoTF has neuroprotective effect** (*12*, *13*)**, but involved mechanisms have not been yet fully elucidated. In this paper, using two RD models, we confirmed that apoTF efficiently removes iron, and exerts anti-oxidant and neuroprotective effect.** However, recent studies have demonstrated that the blockade of apoptosis or necroptosis was required to protect the detached retina (*7*). Using transgenic mice that express human TF in the retina, or using therapeutic regimens with exogenous TF, we demonstrated that TF reduced both the direct iron-mediated necroptosis through RIP kinase down-regulation, as well as the delayed iron-induced apoptosis.

The biologic effects of TF, present at high concentration in the normal vitreous, is not limited to iron metabolism and its neuroprotective properties result from numerous targeted pathways. Lesnikov et al. previously demonstrated that upon binding to the Transferrin receptor 2 (TFR2), TF protected against Fas-induced cell death via the mitochondrial pathway by reducing BID cleavage, inhibiting caspase-3 and -9 activations, and up-regulating survival signals such as Bcl-xL (*26*). The retinal transcriptome of TG RD mice compared with WT RD mice highlighted 7 major groups of pathways regulated by TF: Phagocytosis, Immune systems, Retina homeostasis, Neurological process, Remodeling of the extracellular matrix, Mechanisms of cell death, and Metabolism. TF up-regulated the expression of receptors involved in endocytosis (*Cd36*, *Cd14*, *Siglech*), and down-regulated the expression of vesicle trafficking inhibitors (*Tbc1d14*, *Evi5*, *Tbc1d30*, *Usp6nl*). As a cargo protein, TF facilitates endocytosis/phagocytosis (*27*) and vesicle trafficking (*28*). Amongst the numerous pathways involved in neuroprotection regulated by TF (**table S2**), the IGFBP3 pathway is of particular interest. The up-regulation of IGFBP3 by TF was confirmed at the protein level, and Figure **S8** illustrates IGFBP3 pathways and the genes in this pathway that were up- (red underlined) or down- (green underlined) regulated by TF. The main role of IGFBP3 is to regulate the various functions of IGFs (*29*). Interestingly, when iron levels are high, TF forms complexes with IGFBP3 (*17*), preventing binding to its receptors and subsequent apoptosis and growth inhibition (*29*). IGFBP3-TF complex internalization allows IGFBP3 to be released to cellular organelles (*30*) and mediates neuroprotective effects (*29*, *31*, *32*) (see Fig. **S8** for more details).

From the analysis of ocular fluids of RRD patients, we have demonstrated for the first time the over-saturation of TF and iron overload in a human ocular disease. Despite a high TF concentration in the vitreous, iron accumulates in the retina in other human diseases as observed in Age-related macular degeneration (AMD) (*10*); thus, TF over-saturation could be a general mechanism of PR cell death. Therefore, TF supplementation is a credible strategy for further translational clinical trials in eligible patients. As compared with other iron chelators, TF treatment not only restores iron homeostasis but also activates major neuroprotective pathways such as the IGFBP3 pathway. Future work elucidating the iron-unrelated pathways of TF will be required. We have used retinal detachment as a “model

disease" in which neuroprotective treatments could show functional endpoints in a reasonable time frame. On the basis of the results obtained from experimental models and from human pathology, and because TF is an endogenous molecule, clinical studies should be performed to evaluate TF in conjunction with retinal detachment surgery. Once validated, TF could be proposed as a treatment for other diseases associated with retinal detachment, such as in myopia, or those associated with iron overload such as AMD (*10*).

Materials and Methods

Human samples

Consecutive patients presenting with RRD at Jules-Gonin Eye Hospital (Lausanne, Switzerland) from December 1, 2014, to July 31, 2015, were included according to the protocol approved by the ethics committee and diagnosed through normal standard clinical care at first examination. Upon presentation with RRD, the main inclusion criterion was the necessity of performing intraocular surgery to limit visual impairment, in the absence of other ocular conditions. Among 44 vitreous samples, 35 samples were obtained from patients with macula OFF RD. Nine sex-matched and age-matched patients presented with macular holes (n=4) or with epiretinal membranes (n=5), and no other ocular disease were included during the same period as control subjects for vitreous humor sampling.

Undiluted vitreous samples were collected by manual aspiration through a syringe connected to a 23G vitrectomy cutter (Alcon, Rotkreuz ZG, Switzerland before infusion opening). SRF was collected by active aspiration through a retinal tear (Advanced Backflush DSP cannula, Alcon, Rotkreuz ZG, Switzerland). Samples were coded and stored in a biobank at -80°C until biochemical analysis.

Duration of RRD (mean: 6.7 ± 5.9 days) was defined as the time from the onset of symptoms to surgery. Visual acuities were recorded before and one month after surgery and converted to the logarithm of the minimum angle of resolution (LogMAR). Visual recovery was defined as the difference between post-operative and pre-operative LogMAR visual acuity.

Frozen human post-mortem eye tissues (10 donors) with non-hemorrhagic retinal detachment retrieved from the pathological files of Jules-Gonin Eye Pathology Laboratory were used to stained iron by Perl's

method. A block of tissue ranging from 1 to 1.5 cm long and 0.5 cm wide containing the RD was processed as serial 5 µm-thick paraffin sections.

Animals

Adult male Long-Evans rats (Janvier laboratory, Le Genest St Isle, France) (n=32), adult male Wistar rats (Janvier laboratory) (n=21), adult male C57BL6/J mice (Wild-type (WT)) (Janvier laboratory) (n=40), and adult male transgenic mice expressing human transferrin (TG) (Centre d'exploration fonctionnelle du Centre de Recherche des Cordeliers, UMRS1138, Paris France) (n=40) were fed with a standard laboratory diet and ad libitum tap water in a room maintained at 21-23°C with a 12 h light/dark cycle (6 am-6 pm). Mice were anesthetized with an intraperitoneal injection of ketamine (80 mg/kg; Virbac, Carros, France) and xylazine (12 mg/kg; Bayer, Lyon, France); rats were anesthetized with an intramuscular injection of ketamine (35 mg/kg) and xylazine (5 mg/kg). All animals were sacrificed by carbon dioxide inhalation.

Surgical Induction of RD in rodents and study design

Features of retinal degeneration secondary to detachment were observed in animal models in which the retina is mechanically detached by the subretinal injection of sodium hyaluronate. Once anesthetized Long-Evans rats or WT and TG mice received topical anesthesia with a drop of 1% tetracaïne (Faure, Europhta laboratories, Monaco). Pupil dilatation was obtained by dropwise instillation of 2 mg/0.4 ml mydriaticum (Théa, Clermont-Ferrand, France) and 10% phenylephrine hydrochloride (Faure, Europhta laboratories, Monaco). Retinal detachment was induced by a subretinal injection of 10 µl (mice) or 30 µl (rats) of sodium hyaluronate (5 mg/ml, Healon, Uppsala, Sweden) under an operating microscope using a 34G needle through the sclera **for a total of 50 animals**. The induced retinal detachment occupied approximately 30-70% of the fundus. Eyes with hemorrhagic complications were excluded **(nearly 15%)**. Eyes receiving no injection were used as controls.

Intravitreal injections in rats was performed **immediately** after RD induction with 5 µl of human apo transferrin solution (50 mg/ml in Balanced Salt Solution (BSS), Sigma Aldrich Chemical Co, Saint-Quentin en Yvelines, France) or control solution (BSS) as previously described (*12*).

Fundus and Spectral-Domain Optical coherence tomography (SD-OCT) were simultaneously realized with a Micron III retinal imaging microscope (Phoenix Research Labs, Pleasanton, CA, USA) in anesthetized animals as described, (*12*) before and after RD induction and 4 or 7 days later. At 4 days, some mouse eyes were collected for RNA sequencing (n=4 eyes per group). At 7 days, eyes from rats and mice were collected for histology and immunostaining (n=5 and 7 per group and per analysis for rats and mice, respectively). At 14 days, (5 per group) rat eyes were collected for assay of iron in ocular fluids.

Histology and thickness layers measurement

Fixed eyes were embedded in historesin (Leica, Nanterre, France) to facilitate the cutting of 5 µm-thick sections through the detached area. Sections were stained with 1% Toluidine Blue solution. Sections were observed on a Leitz microscope. Sections with the most detached retinal area were photographed (20X) with a Leica camera for measurements (n=5 WT mice; n=5 TG mice; n=5 BSS-treated rats; n=5 TF-treated rats). Retinal thicknesses (from the outer segments to the inner part of the ganglion cell layer nuclei), the outer nuclear layer (ONL), and the outer and inner segments were measured every 100 µm (mice) and 300 µm (rats) using Image J software by two different blind experimenters. Retinas were considered detached when an empty space was observed between the RPE and the outer segments and attached when any signs of histological disturbance was observed. The retinal thickness ratio was calculated as the thickness in the detached retina/ the thickness in the attached retina. For the ONL and segment thickness ratio, layer measurements were reported as the total retinal thickness of the corresponding retinal area using the formula "(ONL detached/total retina detached)/(ONL attached/total retina attached)".

Immunohistochemistry and fluorescence intensity evaluation

Fixed eyes were mounted in Tissue Tek® O.C.T. (Siemens Medical, Puteaux, France) in order to pass through the detached area. Explants were rinsed in 1X phosphate-buffered saline (PBS, Thermo scientific, Cergy Pontoise, France), fixed for 20 min with 4% paraformaldehyde (PAF, Inland Europe, Conflans sur Lanterne, France), infiltrated in a sucrose gradient series and then, mounted in Tissue Tek

O.C.T. Immunohistochemistry was performed on 10 µm-thick sections as previously described (*12*). Primary antibodies were: rabbit polyclonal anti-TF receptor 1 (Serotec, Oxford, UK), rabbit polyclonal specific for the Light subunit of ferritin (P. Santambrogio); rabbit anti-glial fibrillary acid protein (Dako, Thermo Scientific); rabbit anti-ionized calcium-binding adapter molecule 1 (Iba1, Wako Pure Chemical Industries, Neuss, Germany); mouse anti-CD68 (Bio-Rad AbD Serotec GmbH, Colmar, Fr); anti-8 Hydroxyguanosine (8-HGN, Abcam, Cambridge, UK); anti-4 Hydroxynonenal (4-HNE, Abcam); anti-rhodopsin (Rho4D2, Abcam), anti-cone arrestin (Millipore, Saint Quentin En Yvelines, Fr), and anti-IGFBP3 (Santa Cruz). Control sections were incubated with rabbit non-immune serum (Thermo scientific) or without primary antibodies. The corresponding Alexa–conjugated secondary antibodies (Thermo scientific) were used to reveal the primary antibodies, and sections were counterstained with 4.6-diamidino-2-phenylindole DAPI; Sigma). The terminal deoxynucleotidyl transferase-mediated biotinylated UTP nick end labeling (TUNEL) reaction was performed, along with DAPI staining using the manufacturer's protocol (Roche Diagnostics, Meylan, France) as described (*12*). Propidium iodine at 0.5 µg/ml was incubated directly with sections for one hour and the nuclei were counterstained with DAPI.

The sections were photographed with a fluorescence microscope (BX51, Olympus, Rungis, France) using identical exposure parameters for all compared samples. Blind quantifications were realized on photographs acquired at 40x magnification with Image J software as follows: Quantification of cone nuclei (arrestin staining) or TUNEL positives cells (20x magnifications) in mouse (n=5 per group) or rat (n=5 per group) models of RD was performed using 3 photographs of the attached retina and 3 photographs of the detached retina. Measurement of the outer segment length in rat retina (n=5 per group) was realized in 6 photographs by delimiting Rho4D2 staining and calculating the mean OS length in each retina area. The OS length ratio was then calculated as described for histological measurement. For the explants model, all quantifications were performed on 4 photographs (n=3 explants per group). The OS length measurement was realized by measuring at 3 equidistant points on the photographs. Fluorescence intensity staining was evaluated on photographs and reported as the mean intensity under control conditions. Each sample measurement was averaged and differences between the groups were analyzed.

Retinal explant cultures

Adult Wistar rat retinas were isolated from fresh enucleated eyes, divided into 4 parts, and transferred to 0.2 mm polycarbonate membranes (Millipore) with the ganglion cell layer facing the membrane (**Fig. 2**). Mouse retinal explants were isolated as indicated above, with one explant corresponding to one eye. The insert was placed into a six-well culture plate containing Dulbecco's modified Eagles medium with L-glutamine and 5% serum (Thermo Scientific) corresponding to day 0. To analyze the effects of iron exposure on retinal explants, 30 µl of medium containing $FeSO_4$ ($7H_2O$, Sigma) was added to the photoreceptor side of the explants (upper chamber). To explore transferrin's therapeutic effects, medium in the upper chamber was removed after 2 days; PBS was added for washing, and 30 µl of medium containing 0.5, 5 or 50 mg/ml of human apoTF (Sigma) was placed on the retinas. LDH release and ELISA directed against TF were measured in medium collected from the lower chamber as described previously (*12*, *13*). Histology, iron staining, immunohistochemistry, and western blotting were performed on explants as described below and in the time workflow legends.

Iron status

Vitreous and SRF samples from humans, ocular fluids from RD rats, and medium from rat explants (n=6 per group) were diluted with 1% HNO_3 solution containing 10 ng/mL Rh and 10 ng/mL indium as internal standards. In addition, each analytical batch of study samples was processed with laboratory controls, including method blanks and standard reference materials to continuously monitor method performance. Samples were analyzed using an inductively coupled plasma mass spectrometer (ICP-MS, 7700 Series, Agilent, Santa Clara, CA, USA). Quantitative analysis of iron (Fe) was carried out by external calibration using 7 standards, with concentrations ranging from 10 to 1.000 ng/ml. The method was assessed using internal and external quality controls, analysis of initial calibration, a verification standard, procedural blanks, and duplicate samples.

Transferrin and proteins were quantified using an ELISA kit (AssayPro, St-Charles, USA) and a Micro BCA assay kit (Thermo Scientific), respectively. For human samples, heme iron contamination was

verified with a hemoglobin colorimetric assay **(AssayPro)**. Saturation of transferrin was calculated as the total iron content (µmol/l)/ TIBC (µmol/l). TIBC measures the amount of iron that can potentially be stored in TF and corresponds to the capacity of 1 mol of TF (80,000 Da) to bind 2 mol of ferric iron and was calculated (µmol/l) as: TF concentration (g/l) X 10^6 X (2/80,000).

Iron detection-staining

Perl's reaction staining was performed by incubating in a solution containing 4% potassium ferrocyanide (Sigma) in 4% aqueous hydrochloric acid (Sigma) for 30 min at room temperature to yield a Prussian blue reaction product. Sensitivity for iron detection was enhanced by incubation with a solution of 5 mg/ml 3,3'-Diaminobenzidine Tetrahydrochloride (DAB, Sigma) containing 1% H_2O_2 for 30 min at room temperature. For nucleus counterstaining, incubation with a solution of 1% nuclear red or toluidine blue (Sigma) was performed for 30 s. Stained sections were mounted in aqueous medium. Control of amplification was realized by incubation of sections with DAB without the preceding Perl's reaction step.

Imaging LA-ICP-MS measurements were performed on a quadrupole instrument (Agilent 7700 ICP series, Darmstadt, Germany) hyphenated to a laser ablation system (NWR-213, New Wave, Fremont, USA). Material on tissue sections was ablated by a Nd:YAG/213 nm laser focused at 18 µm diameter prior to transport towards the ICP ion source by a helium carrier gas with a flow-rate of 800 mL/min. The LA-ICP MS parameters were optimized to provide the best signal-to-noise ratio while keeping the maximum reproducibility between analyses. In this way, the energy output was set at 23%, corresponding to a laser fluency of 0.35 J/cm^2. The lateral resolution was fixed at 20 µm in the raster mode with a scan speed and a repetition frequency of 20 Hz and 20 µm/sec, respectively. $^{56}Fe^+$ was monitored for a duty cycle of 1 s. Raw data were acquired using MassHunter software (Agilent, Darmstadt, Germany). Data files (.d) of the IMS experiments were successively converted in mzML and imzML formats using msconvert and imzMLConverter tools, respectively. Ion images were reconstructed and visualized using the MSIReader v0.06 software.

Western blot analysis

Explants (n=4 per group) were suspended in lysis MPER buffer (Thermo Scientific) and then centrifuged for 10 min at 4°C. Protein concentrations were calculated using the Micro BCA protein assay (Thermo Scientific). Five to ten µg of total extract was mixed with protein loading buffer (Thermo Scientific) per manufacturer's instructions. Samples were loaded on 4-12% Bis-Tris gel (Thermo Scientific) and proteins were transferred onto nitrocellulose membranes. Non-specific binding was blocked with 5% non-fat dry milk in Tween/Tris-buffered saline, and then membranes were incubated overnight at 4 °C with the primary antibody against Rhodopsin (1:5,000; Abcam (ab98887)), human TF (1:1,000; Abcam (ab88165), IGFBP3 (clone E9, 1:1,000, Santa Cruz), caspase 3 (clone L-18, 1:500, Santa Cruz), Bcl2 (clone N-19, 1:500, Santa Cruz), RIP (clone 38, 1:500, BD transduction Laboratories), RIP3 (1:1,000, Sigma (PRS2283)), LC3B (1:1,000, Cell Signaling (2775)), or actin (1:4,000, Sigma), followed by incubation with the supplier-recommended dilution of HRP-conjugated secondary antibody for one hour (VectorLabs, Eurobio, Les Ulis, Fr). Protein bands were visualized by an enhanced chemiluminescence reaction (Thermo Scientific) using a BioImaging system (MicroChemi 4.2, Berthold, Fr). The gray values of specific bands were analyzed using Image J and the protein signals of interest were reported relative to the actin signal or to their respective cleaved forms (for caspase 3 and RIP) for each sample.

Real-time RT-PCR

Neural retinas were isolated on ice and directly frozen until RNA isolation. Tissues were homogenized in tubes prefilled with beads (Bertin Technologies, Ozyme, Saint Quentin en Yvelines, Fr) containing RLT lysis buffer (RNeasy mini kit, Qiagen, Courtaboeuf, Fr) for 3 cycles of 30 s at 5,500 rpm in a Precellys Evolution homogenizer (Bertin Technologies). Total RNA was isolated with a RNeasy mini kit (Qiagen, Courtaboeuf, France) according to the manufacturer's protocols. RNA concentration, purity, and integrity were determined with an Agilent Bio-analyzer. All RNA used had an RNA integrity number superior to 8. First-strand cDNA was generated by reverse transcription using 88 ng total RNA and a QuantiTect Reverse Transcription Kit (Qiagen). Quantitative PCR using duplicate technical replicates was performed on a Quant Studio 5 PCR System (Thermo Scientific) using SYBR Green gene

expression assay probes (QuantiTech Primer Assay, Qiagen) of the mouse target genes Caspase 8 (*Casp8*, NM_009812; QT00171437), Insulin-like growth factor binding protein 3 (*Igfbp3*, NM_0008343; QT00493332), an endogenous control Actin b (*Actb*, NM_007393; QT01136772), and QuantiFast SYBR Green PCR Master Mix (Thermo Scientific). The expression levels of individual genes were normalized with *Actb* in the same sample by calculation of the ΔCt value, and relative quantification was performed using the ΔΔCt method with NLE retina serving as a control.

RNA sequencing

Retinas (n=4 per group) were frozen immediately after isolation. Total RNA was extracted using a Precellys Homogenizer (Ozyme, Bertin) and an RNeasy Mini Kit (Qiagen). Samples were sent for sequencing to the iGenSeq transcriptomic platform of the Brain and Spine Institute (Paris, France). The RNA quality was evaluated by capillary electrophoresis (Agilent 2100 Bioanalyzer system) and RNA with integrity numbers (RIN) ranging from 7.8 to 8.2. was accepted for library generation. The cDNA library of each sample was prepared with a KAPA mRNA Hyper Prep (Roche) for 75 bp paired-end reads, according to the manufacturer's instructions. Each of the cDNA libraries was indexed for multiplexing (2x60 million reads/sample), and indexed libraries were sequenced on one lane of the Illumina Nextseq 500 device. Data were recorded in the FASTQ format.

RNA-seq data analysis

RNA-Seq data analysis was performed by GenoSplice technology (www.genosplice.com). Sequencing, data quality, reads repartition (e.g., for potential ribosomal contamination), and insert size estimation were performed using FastQC, Picard-Tools, Samtools and rseqc. Reads were mapped using STARv2.4.0 on the mm10 Mouse genome assembly. A gene expression regulation study was performed as previously described (*33*). Briefly, for each gene present in the Mouse FAST DB v2016_1 annotations, reads aligning on constitutive regions (that are not prone to alternative splicing) were counted. Based on these read counts, normalization and differential gene expression were performed using DESeq2 on R (v.3.2.5). Only genes expressed in at least one of the two compared experimental conditions were further analyzed. Genes were considered as expressed if their rpkm value was greater

than 93% of the background rpkm value, based on intergenic regions. Results were considered statistically significant for uncorrected p-values ≤ 0.05 and fold-changes ≥ 1.5. GenBank accession number: GSE102824.

Pathway/Gene Ontology (GO) analysis and Transcription Factor analysis

Clusterings and heatmaps have been performed on unlabeled data using “dist” and “hclust” functions in R, using Euclidean distance and the Ward agglomeration method. Analysis for enriched GO terms, KEGG pathways and REACTOME pathways were performed using the DAVID Functional Annotation Tool (v6.8). GO terms and pathways were considered enriched if the fold enrichment ≥ 2.0, the uncorrected p-value ≤ 0.05, and the minimum number of regulated genes in the pathway/term ≥ 2.0. Analysis was performed three times: using all regulated genes, using up-regulated genes, and using down-regulated genes only. The union of these three analyses was performed to provide a single list of results. Analysis for transcription factors was performed using orthologous genes between the mouse and the human with the DAVID Functional Annotation Tool (v6.8). Orthologous genes are aggregated in FAST DB from Ensembl compara. The same thresholds and methods were used as GO terms and Pathway analysis but with human data.

Statistical analysis

Results are presented as the mean ± standard error of the mean (SEM). Analyses were performed using GraphPad Prism 5 software. Normal distribution of data was confirmed using the Shapiro–Wilk test. Comparisons between 2 groups of human ocular fluid samples were analyzed by an unpaired two-tailed Student's *t*-test. Multiples comparisons were performed using one-way analysis of variance (ANOVA) followed by the Bonferroni post-test as appropriate. Non-normally distributed data were analyzed using a nonparametric Mann Whitney test to compare the two groups. Unadjusted linear regression and two-tailed Pearson correlation analysis were performed to determine whether a relationship existed between iron concentration and delta logMAR visual acuity or RD duration. $p<0.05$ was considered statistically significant.

Study approval

The study involving human subjects adhered to the tenets of the Declaration of Helsinki and was approved by the local Ethics Committee of the Swiss Department of Health on research involving human subjects (CER-VD N°340/15). For vitreous and sub-retinal fluids, written informed consent was obtained from all patients after detailed explanation of the purpose and methods of the study. All experimental procedures performed using rats and mice were approved by the local ethics committee of the Charles Darwin European Council, University of Paris- Descartes. Experiments were performed in accordance with the Association for Research in Vision and Ophthalmology (ARVO) statement for the use of animals in Ophthalmic and Vision Research.

H2: Supplementary Materials

Supplementary Figure S1: Cell death cellular markers in rat retinal explants exposed to iron

Supplementary Figure S2: Transferrin expression in mouse retinal explants protects from low serum culturing conditions

Supplementary Figure S3: Transferrin expression in mouse retina explants reduced oxidative stress makers induced by iron

Supplementary Figure S4: Transferrin treatment preserves iron-exposed rat retinal explants from oxidative stress and inflammation

Supplementary Figure S5: Animal models of retinal detachment

Supplementary Figure S6: Iron accumulates in the rodent retina following retinal detachment.

Supplementary Figure S7: The expression of the transferrin protein partner, IGFBP3, in mice following retinal detachment

Supplementary Figure S8: Proposed role of IGFBP3 in the protective effect of transferrin

Supplementary Table S1: Top 20 up- and down-regulated genes in TG compared with WT mice following retinal detachment

Supplementary Table S2: Pathways and genes regulated by Transferrin and implicated in photoreceptors rescues

Supplementary Data file S1: Complete transcriptomic analysis.

References and Notes

REFERENCES

1. Y. Murakami *et al.*, Photoreceptor cell death and rescue in retinal detachment and degenerations. *Prog Retin Eye Res*. **37**, 114–140 (2013).

2. M. A. J. Van de Put, J. M. M. Hooymans, L. I. Los, Dutch Rhegmatogenous Retinal Detachment Study Group, The incidence of rhegmatogenous retinal detachment in The Netherlands. *Ophthalmology*. **120**, 616–622 (2013).

3. B. A. Holden *et al.*, Global Prevalence of Myopia and High Myopia and Temporal Trends from 2000 through 2050. *Ophthalmology*. **123**, 1036–1042 (2016).

4. D. Mitry *et al.*, Long-term visual acuity and the duration of macular detachment: findings from a prospective population-based study. *Br. J. Ophthalmol.* **97**, 149–152 (2013).

5. M. A. J. van de Put *et al.*, Postoperative vision-related quality of life in macula-off rhegmatogenous retinal detachment patients and its relation to visual function. *PLoS ONE*. **9**, e114489 (2014).

6. D. H. Anderson, W. H. Stern, S. K. Fisher, P. A. Erickson, G. A. Borgula, Retinal detachment in the cat: the pigment epithelial-photoreceptor interface. *Invest. Ophthalmol. Vis. Sci.* **24**, 906–926 (1983).

7. G. Trichonas *et al.*, Receptor interacting protein kinases mediate retinal detachment-induced photoreceptor necrosis and compensate for inhibition of apoptosis. *Proc. Natl. Acad. Sci. U.S.A.* **107**, 21695–21700 (2010).

8. G. P. Lewis, C. J. Guérin, D. H. Anderson, B. Matsumoto, S. K. Fisher, Rapid changes in the expression of glial cell proteins caused by experimental retinal detachment. *Am. J. Ophthalmol.* **118**, 368–376 (1994).

9. R. Eid, N. T. T. Arab, M. T. Greenwood, Iron mediated toxicity and programmed cell death: A review and a re-examination of existing paradigms. *Biochim. Biophys. Acta, Mol. Cell Res.* **1864**, 399–430 (2017).

10. X. He *et al.*, Iron homeostasis and toxicity in retinal degeneration. *Prog. Retin. Eye Res.* **26**, 649–673 (2007).

11. E. Picard *et al.*, The protective role of transferrin in Muller glial cells after iron-induced toxicity. *Mol. Vis.* **14**, 928–941 (2008).

12. E. Picard *et al.*, Targeting iron-mediated retinal degeneration by local delivery of transferrin. *Free Radic. Biol. Med.* **89**, 1105–1121 (2015).

13. E. Picard *et al.*, Overexpressed or intraperitoneally injected human transferrin prevents photoreceptor degeneration in rd10 mice. *Mol. Vis.* **16**, 2612–2625 (2010).

14. J. Winkler, H. Hoerauf, The retinal organ culture-a model system for the examination of the early cytoskeletal reaction pattern after retinal detachment. *Klin. Monbl. Augenheilkd.* **225**, 269–275 (2008).

15. H. Matsumoto, J. W. Miller, D. G. Vavvas, Retinal detachment model in rodents by subretinal injection of sodium hyaluronate. *J. Vis. Exp.* (2013), doi:10.3791/50660.

16. G. P. Lewis, S. K. Fisher, Up-regulation of glial fibrillary acidic protein in response to retinal injury: its potential role in glial remodeling and a comparison to vimentin expression. *Int. Rev. Cytol.* **230**, 263–290 (2003).

17. G. Miljuš, V. Malenković, B. Đukanović, N. Kolundžić, O. Nedić, IGFBP-3/transferrin/transferrin receptor 1 complexes as principal mediators of IGFBP-3 delivery to colon cells in non-cancer and cancer tissues. *Exp. Mol. Pathol.* **98**, 431–438 (2015).

18. M. Cederlund, F. Ghosh, K. Arnér, S. Andréasson, B. Åkerström, Vitreous levels of oxidative stress biomarkers and the radical-scavenger α1microglobulin/A1M in human rhegmatogenous retinal detachment. *Graefes Arch. Clin. Exp. Ophthalmol.* **251**, 725–732 (2013).

19. B. Baumann *et al.*, Conditional Müller Cell Ablation Leads to Retinal Iron Accumulation. *Invest. Ophthalmol. Vis. Sci.* **58**, 4223–4234 (2017).

20. J. C. Jeanny *et al.*, Iron and regulatory proteins in the normal and pathological retina. *Bull. Acad. Natl. Med.* **197**, 661–74 (2013).

21. M. H. Guajardo, A. M. Terrasa, A. Catala, Lipid-protein modifications during ascorbate-Fe2+ peroxidation of photoreceptor membranes: protective effect of melatonin. *J. Pineal Res.* **41**, 201–210 (2006).

22. D. Devos *et al.*, Targeting chelatable iron as a therapeutic modality in Parkinson's disease. *Antioxid. Redox Signal.* **21**, 195–210 (2014).

23. N. Parakh *et al.*, Neurological Complications and Cataract in a Child With Thalassemia Major Treated With Deferiprone. *J. Pediatr. Hematol. Oncol.* **37**, e433-434 (2015).

24. M. Di Nicola, G. Barteselli, L. Dell'Arti, R. Ratiglia, F. Viola, Functional and Structural Abnormalities in Deferoxamine Retinopathy: A Review of the Literature. *Biomed Res Int*. **2015**, 249617 (2015).

25. N. Mobarra *et al.*, A Review on Iron Chelators in Treatment of Iron Overload Syndromes. *Int J Hematol Oncol Stem Cell Res*. **10**, 239–247 (2016).

26. V. A. Lesnikov, M. P. Lesnikova, H. J. Deeg, Neuroimmunomodulation and aging: a role for transferrin and the hypothalamus/thymus axis. *Curr. Aging Sci.* **6**, 21–28 (2013).

27. H. Sakamoto *et al.*, A novel function of transferrin as a constituent of macromolecular activators of phagocytosis from platelets and their precursors. *Biochem. Biophys. Res. Commun.* **230**, 270–274 (1997).

28. A. Longatti *et al.*, TBC1D14 regulates autophagosome formation via Rab11- and ULK1-positive recycling endosomes. *J. Cell Biol.* **197**, 659–675 (2012).

29. M. A. Johnson, S. M. Firth, IGFBP-3: A cell fate pivot in cancer and disease. *Growth Horm. IGF Res.* **24**, 164–173 (2014).

30. S. Storch *et al.*, Transferrin binds insulin-like growth factors and affects binding properties of insulin-like growth factor binding protein-3. *FEBS Lett.* **509**, 395–398 (2001).

31. R. C. Baxter, Nuclear Actions of Insulin-like Growth Factor Binding Protein-3. *Gene*. **569**, 7–13 (2015).

32. K.-W. Lee *et al.*, Cellular internalization of insulin-like growth factor binding protein-3: distinct endocytic pathways facilitate re-uptake and nuclear localization. *J. Biol. Chem.* **279**, 469–476 (2004).

33. L. Noli, A. Capalbo, C. Ogilvie, Y. Khalaf, D. Ilic, Discordant Growth of Monozygotic Twins Starts at the Blastocyst Stage: A Case Study. *Stem Cell Rep.* **5**, 946–953 (2015).

34. D. Cosgrove, M. Zallocchi, Usher protein functions in hair cells and photoreceptors. *Int J Biochem Cell Biol*. **46**, 80–89 (2014).

35. P. A. Williams, C. E. Braine, N. E. Foxworth, K. E. Cochran, S. W. M. John, GlyCAM1 negatively regulates monocyte entry into the optic nerve head and contributes to radiation-based protection in glaucoma. *Journal of Neuroinflammation*. **14** (2017), doi:10.1186/s12974-017-0868-8.

36. M. Gold *et al.*, α 1-antitrypsin modulates microglial-mediated neuroinflammation and protects microglial cells from amyloid-β-induced toxicity. *Journal of Neuroinflammation*. **11** (2014), doi:10.1186/s12974-014-0165-8.

37. M. Lee, S. Li, K. Sato, M. Jin, Interphotoreceptor Retinoid-Binding Protein Mitigates Cellular Oxidative Stress and Mitochondrial Dysfunction Induced by All-trans-Retinal. *Invest. Ophthalmol. Vis. Sci.* **57**, 1553–1562 (2016).

38. V. Higenell, E. S. Ruthazer, Layers upon layers: MHC class I acts in the retina to influence thalamic segregation. *Neuron*. **65**, 439–441 (2010).

39. H. Matsumoto *et al.*, Strain Difference in Photoreceptor Cell Death After Retinal Detachment in Mice. *Invest. Ophthalmol. Vis. Sci.* **55**, 4165–4174 (2014).

40. C. R. Elliott-Hunt *et al.*, Endogenous galanin protects mouse hippocampal neurons against amyloid toxicity in vitro via activation of galanin receptor-2. *J. Alzheimers Dis.* **25**, 455–462 (2011).

41. Y. Inoue *et al.*, Protective effects of placental growth factor on retinal neuronal cell damage. *J. Neurosci. Res.* **92**, 329–337 (2014).

42. A. S. Coyner *et al.*, Retinal Neuroprotective Effects of Flibanserin, an FDA-Approved Dual Serotonin Receptor Agonist-Antagonist. *PLOS ONE*. **11**, e0159776 (2016).

43. A. Maeda *et al.*, Effects of Potent Inhibitors of the Retinoid Cycle on Visual Function and Photoreceptor Protection from Light Damage in Mice. *Mol Pharmacol*. **70**, 1220–1229 (2006).

Acknowledgments

General:

We thank Drs. Yves Courtois, Alicia Torriglia, Imène Jaadane and Marc Abitbol (UMRS1138, Centre de Recherche des Cordeliers, INSERM) for their guidance, stimulating discussion and manuscript reviews. We thank the Institut du cerveau et de la Moelle épinière – ICM (Plateforme de Séquençage – iGenSeq; Hôpital de la Salpetrière) for RNA sequencing, and Genosplice for data analysis. The authors wish to thank Paolo Santambrogio (Department of Biological and Technological Research, Instituto de Ricovero e Cure a Carattere Scientifico, San Rafaelle, Milan, Italy) for the rabbit polyclonal antibody specific for the High and Light subunits of Ferritin. And we also wish to thank MSGraphique and Sébastien Maroillez) for illustrations.

Funding:

This study was supported by INSERM, ANR JCJC 2015 Transfiron, and NIH P30EY006360, VA RR&D I21RX001924 and C9246C, Research to Prevent Blindness, Inc., and the Abraham J. & Phyllis Katz Foundation. We would like to thank Editage (www.editage.com) for English language editing.

Author contributions:

AD: conducting experiments and surgeries, acquiring data, analyzing data, and writing the manuscript.

QLR: conducting immunohistochemistry studies and PCR experiments and acquiring data.

LJ: conducting histological experiments.

MCN: conducting histological and animal experiments.

LK: human samples biobank manager.

JAP: conducting surgeries, acquiring data.

JHB: conducting experiments, analyzing data, and writing the manuscript

AT: conducting iron assay experiments.

NT: conducting transferrin assay experiments.

AM: conducting human iron staining experiments.

FBC: designing research studies, conducting experiments, analyzing data, and writing the manuscript.

EP: designing research studies, conducting experiments, acquiring data, analyzing data, and writing the manuscript.

Competing interests: The authors declare no competing interests.

Data and materials availability: GenBank accession number: GSE102824.

Figures and Tables

Figure 1:

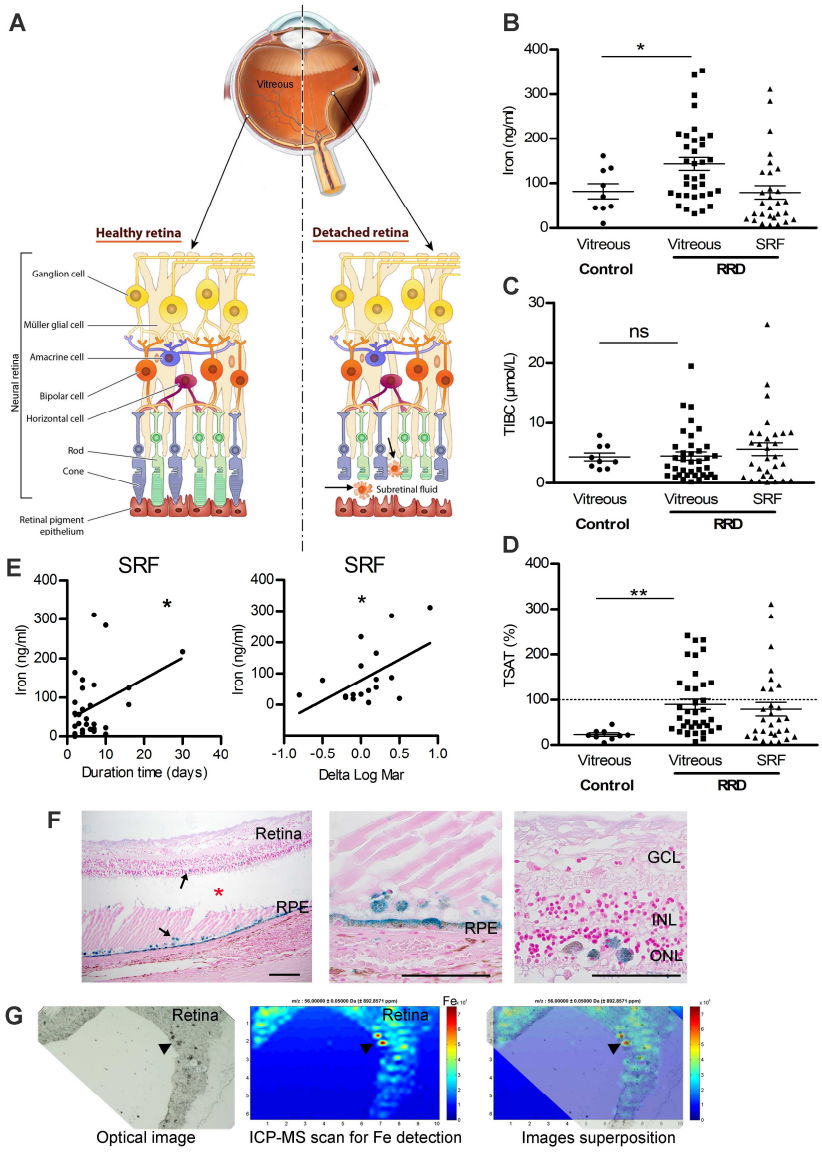

Figure 1: Iron accumulates during retinal detachment in humans

(A) Schematic representation of rhegmatogenous retinal detachment. Retinal pigment epithelium (RPE) strictly interacted with photoreceptors (rods and cones), supporting their function and maintaining retinal physiology. During rhegmatogenous retinal detachment (RRD), separation of the neural retina from the RPE disrupts the metabolism of photoreceptors and induces permanent cellular damage and subretinal fluid (SRF) accumulation through the retinal tear (arrowhead). **(B-D)** Iron level (A), Total Iron binding capacity (TIBC) (B) and Transferrin Saturation (TSAT) (C) were quantified in vitreous from control patients and in vitreous and SRF from RRD patients. Unpaired t test (n= 9-35 for vitreous,

and n=30 for SRF), *p= 0.046; **p=0.006. **(E)** Iron level in SRF was correlated to duration of the RRD (n=30) and to the visual recovery one month following surgical treatment (n=10). Pearson correlation test, *p<0.05. **(F)** Perl's staining (blue) on retinal sections from patients with non-hemorrhagic retinal detachment (asterisk shows space between retina and underlying RPE) revealed iron deposits in the retina and the RPE (arrows). **(G)** Iron distribution map realized by Inductively Coupled Plasma Mass Spectrometry on the retina from a patient with non-hemorrhagic retinal detachment revealed iron deposits (arrowheads). An optical image of the analyzed retina section (left), and the corresponding ICP-MS image of Fe distribution (medium) and the superposition of both (right). The color spectrum represents an ion intensity map of Fe. SFR: Subretinal fluid; RRD: Rhegmatogenous retinal detachment, GCL: Ganglion cell layer; INL: Inner nuclear layer; ONL: Outer nuclear layer; RPE: Retinal pigmented epithelium. Scale bars: 500 µm. All values are represented as the mean ±SEM.

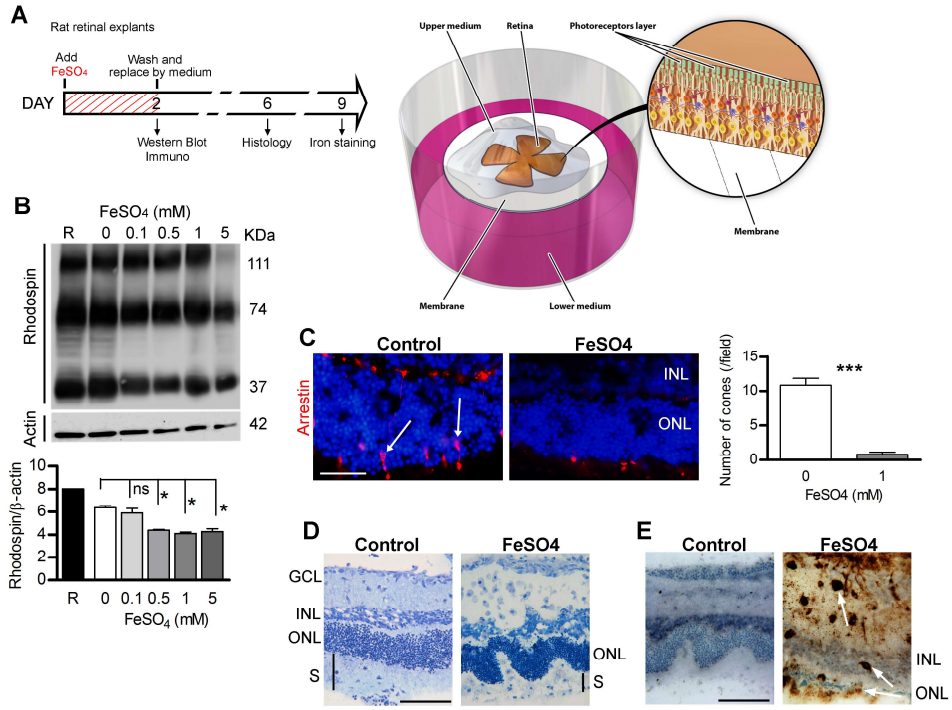

Figure 2: Iron toxicity for photoreceptors in rat retinal explants

(A) Illustration of the retinal explant model and the timed workflow for iron exposure protocol: Adult rat retinas were dissected, placed on membranes with photoreceptors facing up and immediately exposed for two days to iron ($FeSO_4$). Control explants were cultured with medium alone. Some explants were harvested and western blotting and Immunostaining were performed. Afterwards, the medium was completely replaced and explants maintained in culture for 4 or 7 days for histological analysis and iron staining, respectively. **(B)** Western blotting and quantitative analysis of a rod protein showed a decreased rhodopsin level in explants exposed with increasing concentration of $FeSO_4$. The molecular masses of the immunolabeled fragments were indicated in the right margin. Mann Whitney test (n=3, *p=0.028). **(C)** Immunostaining of arrestin (red, arrows) and subsequent quantification showed very few cones present in explants exposed to 1 mM of $FeSO_4$. Mann Whitney test (n=3, ***p<0.0001). **(D)** Semi-thin sections of explants showed disorganization of the outer nuclear layer and segments after 1 mM $FeSO_4$ exposure. **(E)** 3,3′-Diaminobenzidine (DAB) amplified Perl's reaction revealed iron deposits (arrows) in explants exposed to 1 mM $FeSO_4$. GCL: Ganglion cell layer; ONL: Outer nuclear layer; INL: Inner nuclear layer; S: Segments. Scale bars: 100 µm. All values are represented as the mean ± SEM.

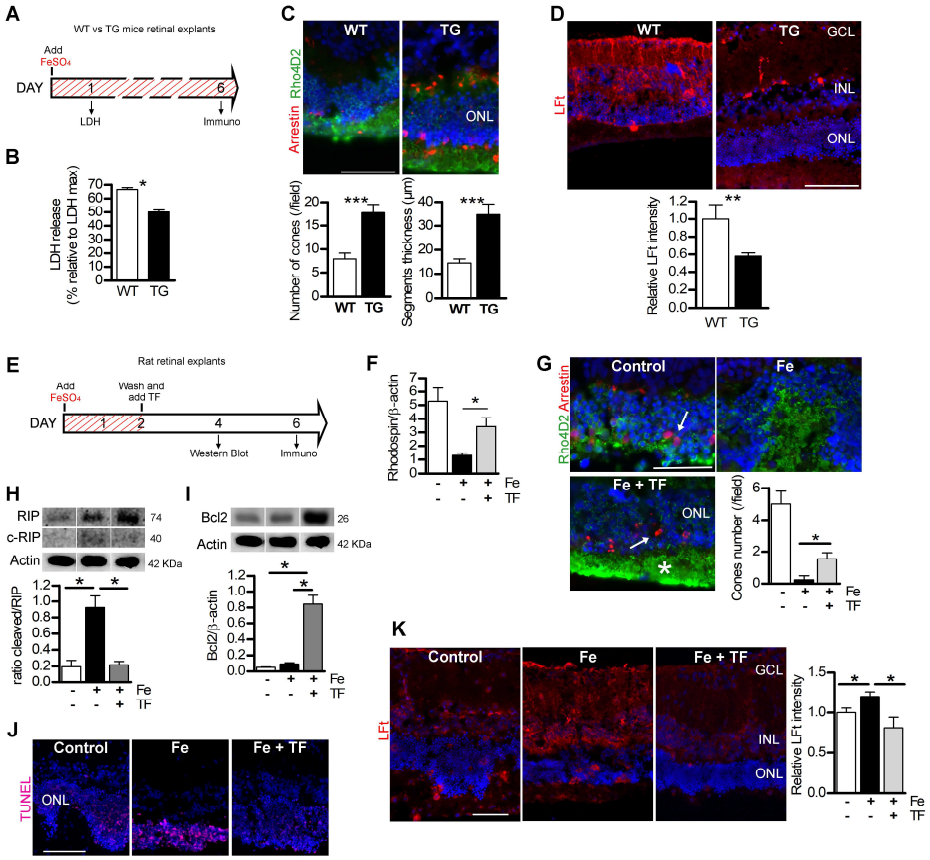

Figure 3: Expression of transferrin protects retina explants exposed to iron

(A) Illustration of timed workflow for retinal explants from wild-type (WT) and transgenic mice (TG) expressing human transferrin (TF) continuously exposed to 1 mM of $FeSO_4$. LDH release was measured after 1 day and immunostaining after 6 days. **(B)** LDH release was lower in culture medium from TG explanted mice compared to WT explants. Mann Whitney test (n=6), *p=0.03. **(C)** Number of cones, stained by arrestin (arrow) and length of rod segments, stained by rhodopsin (rho4D2) were quantified and were higher in TG explants. Mann Whitney test (n=3), ***p<0.001. **(D)** Quantification of immunostaining intensity for markers of iron storage, ferritin light chain was decreased in TG explants compared with WT explants. Mann Whitney test (n=3), **p<0.01. **(E)** Illustration of timed workflow for transferrin (TF) treatment on iron-exposed explants: Adult rat retinas were exposed for 2 days with 1 mM $FeSO_4$. Control explants were cultured with medium alone. Afterwards, the medium was completely replaced and explants were treated with 50 mg/ml of human TF for 2 or 4 days. **(F)** Quantitative analysis of rhodopsin protein by Western blotting show increased rhodopsin protein expression in TF-treated iron-exposed explants (Fe+TF). Mann Whitney test (n=3), *p=0.021. **(G)**

Rhodopsin and arrestin immunostaining revealed protection of rod segments (Rho4D2, asterisk) and cones (arrow) by TF treatment (Fe+TF). Quantification of cone nuclei showed more cones in explants treated with TF than those exposed to $FeSO_4$. Mann Whitney test (n=3), *p=0.036. **(H)** Western blotting and quantitative analysis of receptor-interacting protein kinase (RIP) demonstrated higher full-form and cleaved form of the proteins in iron-exposed retinal explants. The cleaved form of RIP reported on RIP full form was reduced when TF was used to treated iron-exposed explants. Mann Whitney test (n=3), *p=0.028. **(I)** Anti-apoptotic Bcl2 protein, detected by western blotting, was increased in TF-treated iron-exposed explants. Mann Whitney test (n=3), *p=0.028. **(J)** TUNEL positive cells in the outer nuclear layer was reduced by TF treatment. **(K)** Immunostaining of iron storage marker, ferritin light chain was significantly lower in explants treated with TF (Fe+TF) than without treatment (Fe). Fluorescence intensity was reported relative to control conditions. One- way ANOVA, Bonferroni post-test (n=3), *p<0.05. GCL: Ganglion cell layer; ONL: Outer nuclear layer; INL: Inner nuclear layer. Scale bars: 100 µm. All values are represented as mean ±SEM.

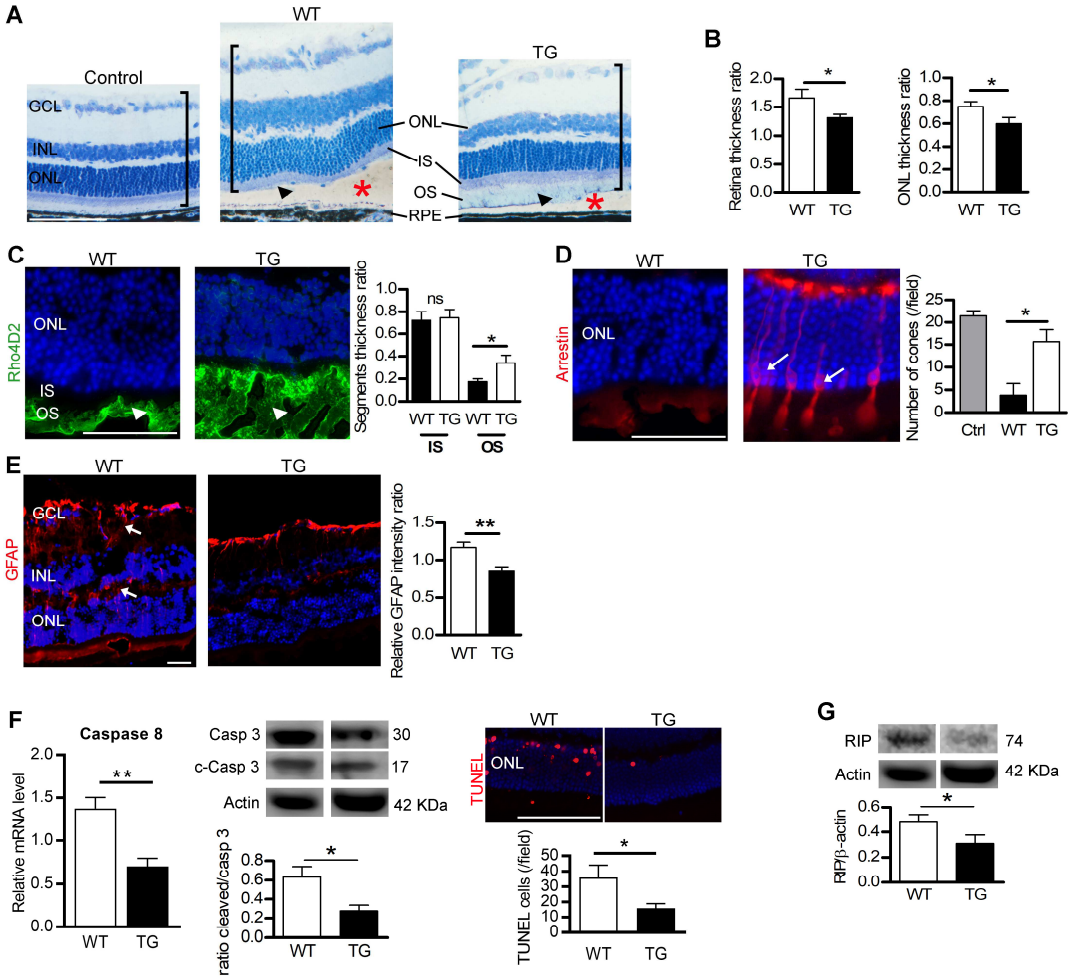

Figure 4: Transferrin expression preserves the detached retina in mice

(A) Semi thin retinal sections from control wild-type (WT) mice without RD, and WT and transgenic mice (TG) mice expressing human transferrin (TF) 7 days after retinal detachment (RD) (red asterisks). In TG mice, the histology of the detached retina (brackets) was less disrupted than in WT mice, with remaining OS (arrowheads). Nuclei were stained with toluidine blue. Measurements of total retinal thickness in the detached area was reported to undetached retina thickness. **(B)** Expression of human TF in mice (TG), reduced thickening of the total retina, and ONL. Mann Whitney test (n=5), *p<0.05, ns: not significant. **(C)** Rhodopsin staining in OS was conserved in TG compared with WT mice (arrowheads) 7 days after RD. The length of OS measured on semi-thin sections was higher in TG mice compared with WT mice. Mann Whitney test (n=6), *p=0.047 **(D)** Arrestin staining revealed cones in retinal sections of TG mice (arrows) 7 days after RD. Cone number was higher in TG compared with WT mice. Mann Whitney test (n=6), *p=0.025. **(E)** Müller glial cell activation revealed by GFAP

expression was lower in TG mice compared with WT mice (arrows). Mann Whitney test (n=5), **p=0.0056. **(F)** Cellular markers of apoptosis were lower in TG compared to WT mouse retinas. Caspase 8 mRNA level by RT-qPCR, and the ratio of cleaved/pro-caspase 3 protein levels by western blotting was performed 4 days after RD. TUNEL staining was performed in eyes collected 7 days after RD. Mann Whitney test (n=5), ** p=0.008, *p=0.028. **(G)** Necrotic RIP kinase protein level, detected by western blotting was reduced in TG mice compared with WT mice. Mann Whitney test (n=3), *p=0.028. GCL: Ganglion cell layer; INL: Inner nuclear layer; IS: Inner segment; ONL: Outer nuclear layer; OS: Outer segment; RPE: Retinal pigmented epithelium. Scale bars: 100 µm (A, E, F); 50 µm (C-D). All values are represented as the mean ± SEM.

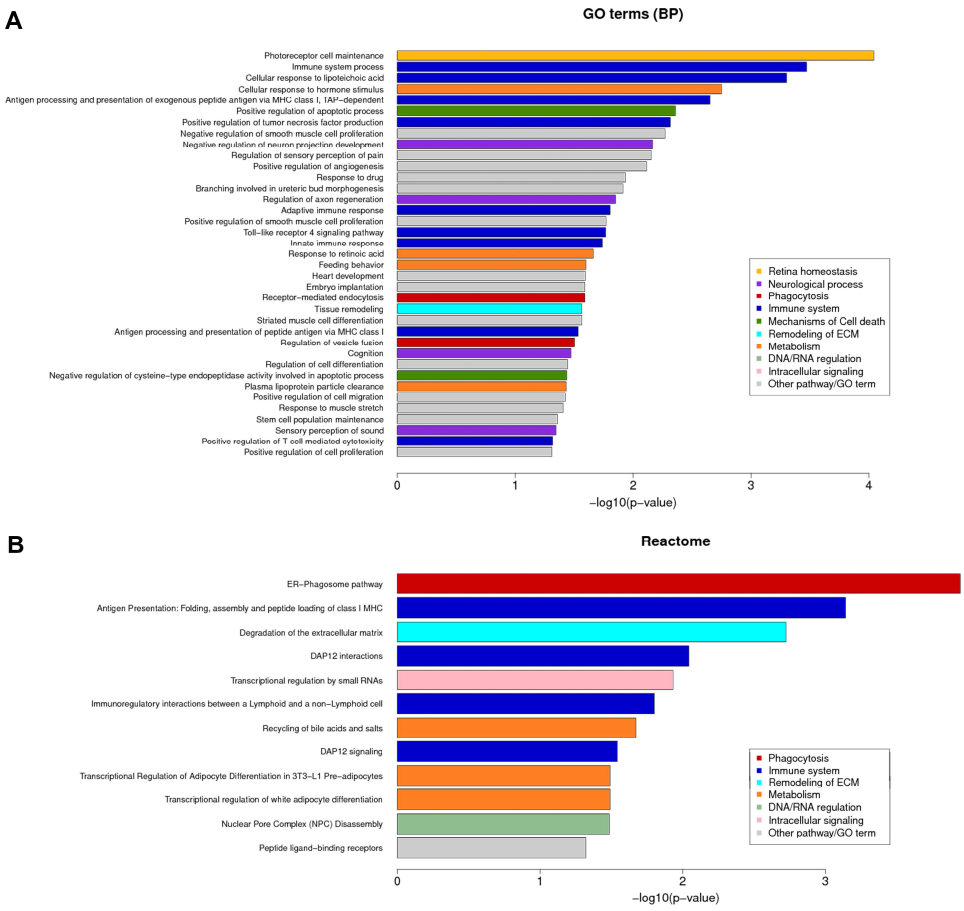

Figure 5: High-throughput analyses of the transcriptome of TG mouse retinas following retinal detachment.

Over-representation pathway analysis using gene ontology (GO) terms enrichment (biological process clustering) (**A**) and reactome biosource (**B**). Color codes were used to associate pathways with common biological effects. Comparatives analysis were done in TG versus WT retinas 4 days after retinal detachment (n=4). GO terms and pathways were considered as enriched if fold enrichment $\geq$ 2.0, uncorrected p-value $\leq$ 0.05, and the minimum number of regulated genes in pathway/term $\geq$ 2.0.

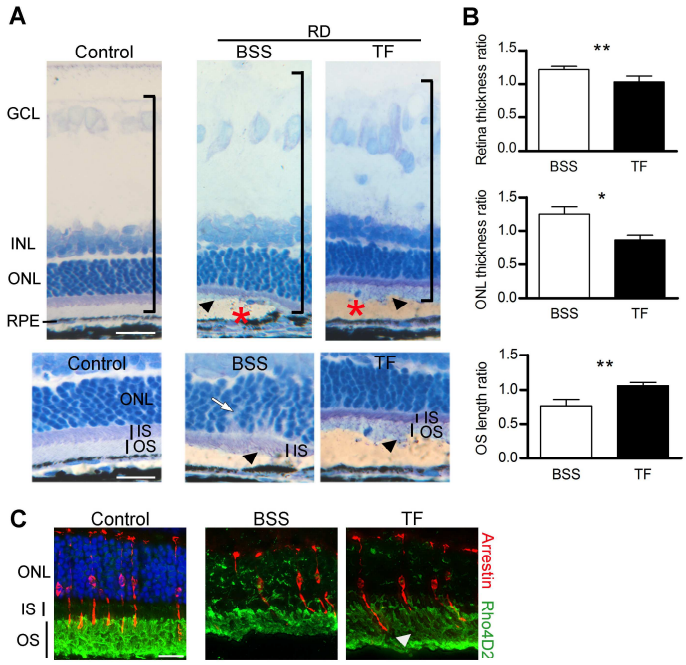

Figure 6: Local administration of transferrin preserves neural retina in the rat model of retinal detachment.

(A) Rat semi-thin retinal sections without retinal detachment (RD) (control) and with RD, treated either by intravitreal injection of a control solution (BSS) or transferrin (TF, 50 mg/ml). Retinal histology in the detached area (asterisks) was more preserved in animals treated with TF compared with those receiving BSS. Higher magnifications showed less ONL disorganization (arrow) and longer outer segments (arrowheads) in TF-treated RD rats. Nuclei were stained with toluidine blue. Measurements of thickness in detached retinas was reported relative to undetached retina thickness. **(B)** Treatment with TF reduced thickening of the total retina and the outer nuclear layer. Mann Whitney test (n=5), *p=0.013; **p≤0.01; ns: not significant. The length of outer segments (OS) was higher in TF-injected RD rats. Mann Whitney test (n=5), **p=0.007. **(C)** Rhodopsin (green) and arrestin (red) staining in rats 7 days after RD. OS were preserved in TF-treated animals (arrowhead). GCL: Ganglion cell layer; INL: Inner nuclear layer; IS: Inner segment; ONL: Outer nuclear layer; OS: Outer segment; RPE: Retinal pigmented epithelium. Scale bars: 20 µm (A, C), 50 µm (A, high magnification). All values are represented as the mean ± SEM.

Supplementary Materials

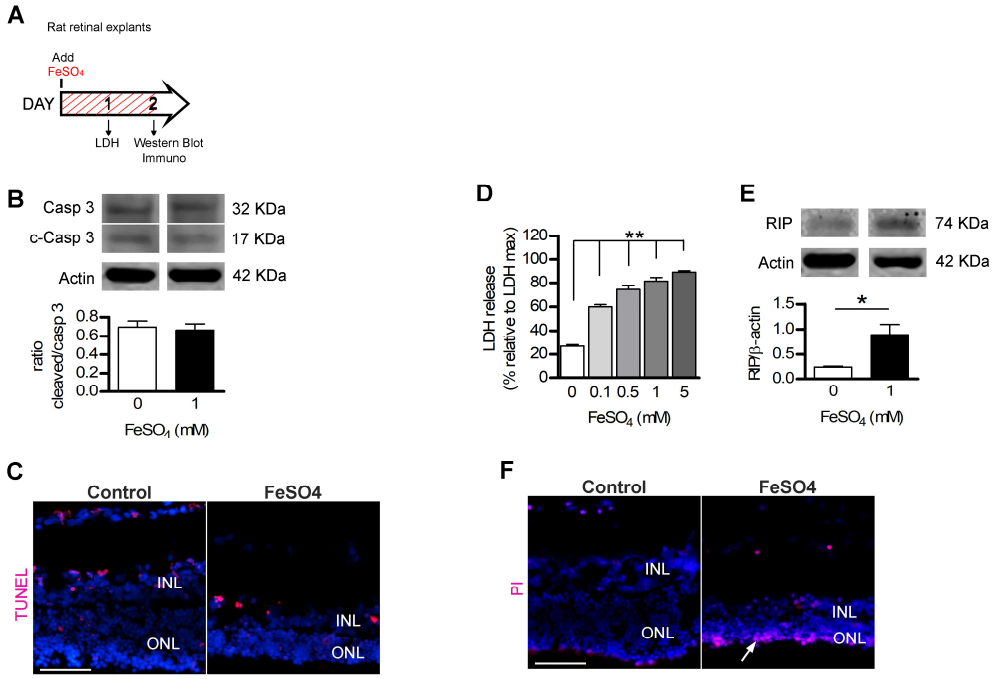

Supplementary Figure 1: Cell death cellular markers in rat retinal explants exposed to iron

(A) Timed workflow of rat retinal explants exposed to 1 mM $FeSO_4$ for 2 days. **(B)** Western blot and quantitative analysis of cleaved caspase 3 protein reported relative to pro-caspase 3 protein expression (n=3). **(C)** The absence of the apoptotic nucleus, marked with TUNEL, in control and iron-exposed explants. **(D)** After one day of exposure, an early necrotic marker, lactate dehydrogenase (LDH) released in the medium, was increased according to the iron ($FeSO_4$) concentration. Mann Whitney test (n=6), **p=0.002 compared to explants without iron exposure. **(E)** Western blot and quantitative analysis of RIP3 protein reported relative to actin protein expression. Mann Whitney test (n=3), *p=0.028. **(F)** Necrotic nuclei stained with propidium iodide (PI) were only observed in iron-exposed retinal explants. ONL: Outer nuclear layer; INL: Inner nuclear layer. Scale bars: 50 µm. All values are represented as the mean ± SEM.

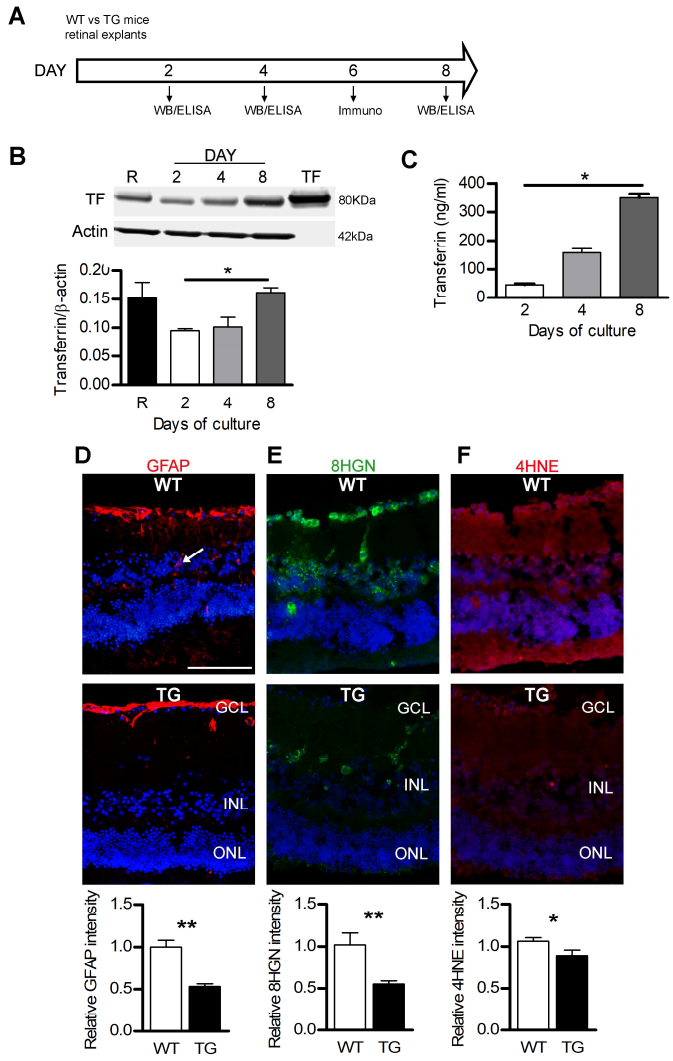

Supplementary Figure 2: Transferrin expression in mouse retinal explants protects from low serum culturing conditions

(A) Illustration of the timed workflow for retinal explants from wild-type (WT) and transgenic mice (TG) expressing human transferrin (TF): mouse retinas were dissected and placed in culture. Quantification of TF levels was performed by western blotting and ELISA at day 2, 4 and 8. Effects of culture conditions on retinal explants were evaluated by immunostaining at day 6. **(B)** Western blotting and quantitative analysis of TF in retinas of TG mice following 2, 4 or 8 days of culture. Mann Whitney test (n=3, *p=0.04). **(C)** Release of TF in culture medium of TG retinal explants increased with days of culture. Mann Whitney test (n=6, *p=0.04). **(D-F)** TF decreased immunostaining of markers characterizing Müller glial cell activation (D, Glial fibrillary acidic protein, arrows), DNA damage (E, 8-Hydroxyguanosine), lipid peroxidation (F, 4-Hydroxynonenal). Measurements of staining intensity

were reported relative to WT explants. Mann Whitney test (n=3), *p<0.05; **p<0.01; **p<0.001. GCL: Ganglion cell layer; ONL: Outer nuclear layer; INL: Inner nuclear layer; S: Segments. Scale bar: 100 µm. All values are represented as the mean ± SEM. R= Retina.

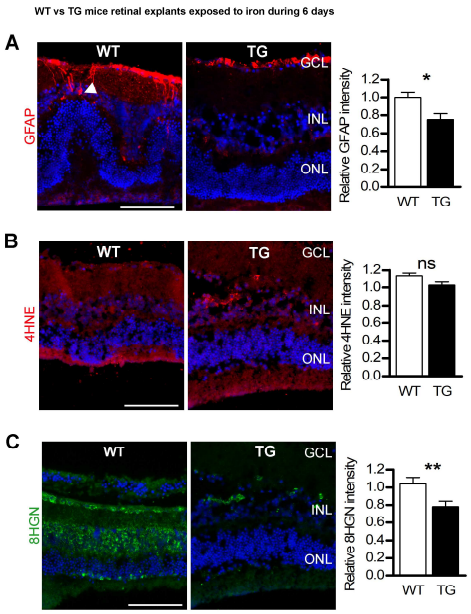

Supplementary Figure 3: Transferrin expression in mouse retina explants reduced oxidative stress makers induced by iron

Retinal explants from wild-type (WT) and transgenic mice (TG) expressing human transferrin (TF) were exposed to 1 mM of $FeSO_4$ during 6 days. Quantification of immunostaining intensity for markers of Müller glial cell activation (**A**, Glial fibrillary acidic protein, arrows), lipid peroxidation (**B**, 4-hydroxynonenal), and DNA damage (**C**, 8-hydroxyguanosine) were decreased in TG explants compared with WT explants. Mann Whitney test (n=3), *p<0.05; **p<0.01; ns: not significant. GCL: Ganglion cell layer; ONL: Outer nuclear layer; INL: Inner nuclear layer. Scale bars: 100 µm All values are represented as the mean ± SEM.

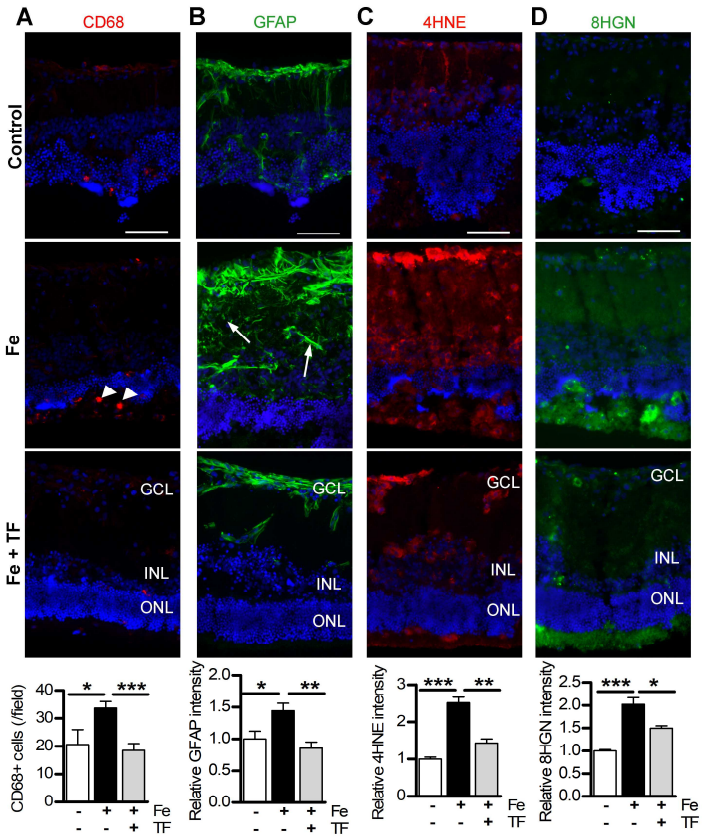

Supplementary Figure 4: Transferrin treatment preserves iron-exposed rat retinal explants from oxidative stress and inflammation

Adult rat retinas were exposed for 2 days with 1 mM $FeSO_4$. Afterwards, the medium was completely replaced and explants were treated with 50 mg/ml of human TF for 4 days. Control explants were cultured with medium alone. Immunostaining of activated macrophages/microglia (**A**, CD68, arrowheads), Müller glial cells activation (**B**, Glial fibrillary acidic protein), lipid peroxidation (**C**, 4-Hydroxynonenal), and DNA damage (**D**, 8-Hydroxyguanosine) were significantly lower in explants treated with TF (Fe+TF) than without treatment (Fe). Fluorescence intensity was reported relative to control conditions. One-way ANOVA, Bonferroni post-test (n=3), *p<0.05; **p<0.01; ***p<0.001. GCL: Ganglion cell layer; ONL: Outer nuclear layer; INL: Inner nuclear layer. Scale bars: 100 µm. All values are represented as mean ±SEM.

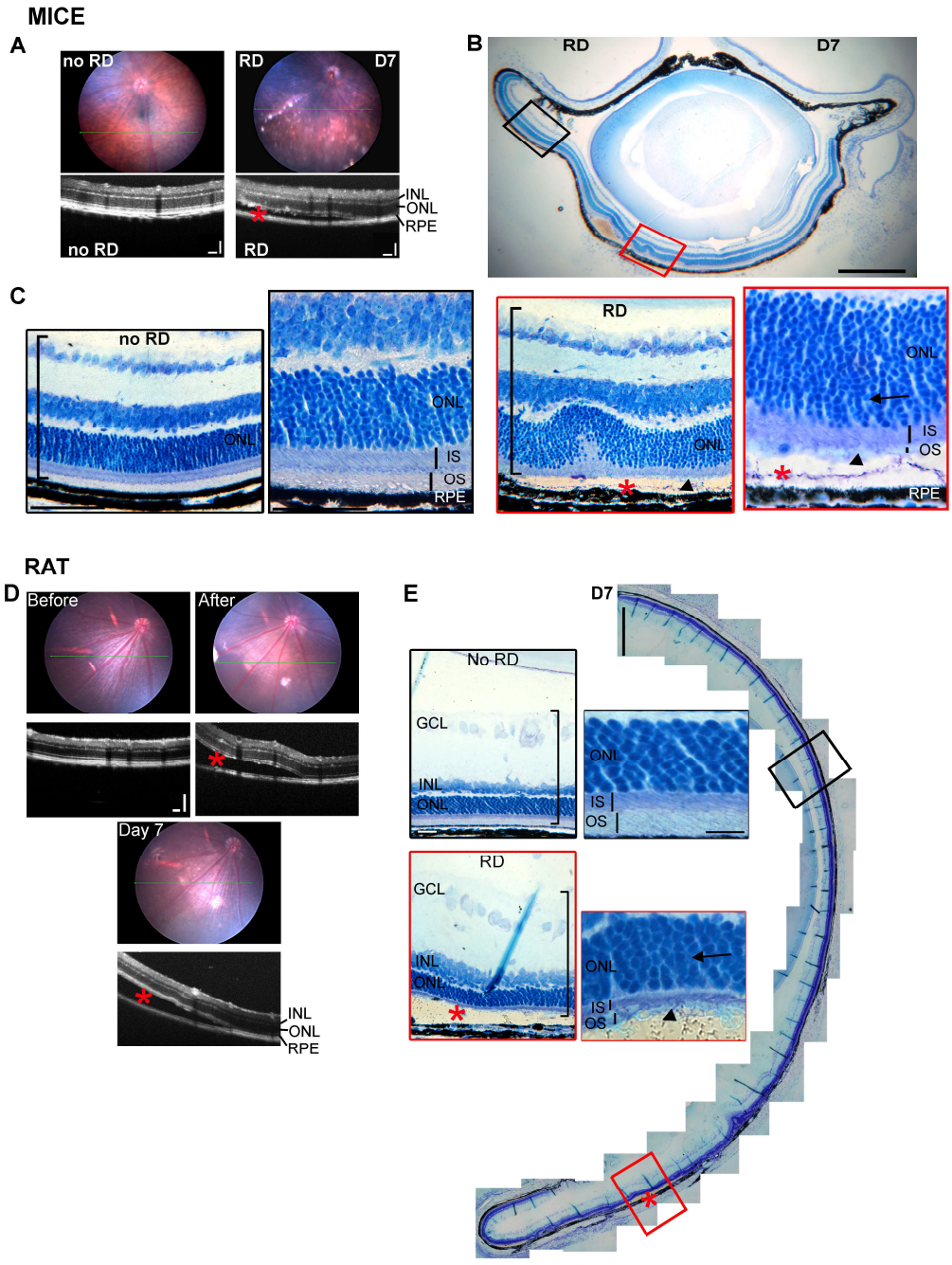
MICE
A
no RD
RD
D7
INL
ONL
RPE
no RD
RD
B
RD
D7
C
no RD
ONL
ONL
IS
OS
RPE
RD
ONL
ONL
IS
OS
RPE
RAT
D
Before
After
Day 7
INL
ONL
RPE
E
D7
No RD
GCL
INL
ONL
ONL
IS
OS
RD
GCL
INL
ONL
ONL
IS
OS

Supplementary Figure 5: Animal models of retinal detachment

(A-C) The mouse model of retinal detachment (RD). (A) Representative fundus photographs and the corresponding optical coherence tomography (OCT) images from a control eye (no RD, left) and an eye with RD 7 days after induction (red asterisk shows subretinal space, right). **(B)** Retinal semi-thin sections 7 days after RD showing the detached area. The red box denotes the detached area and the black box denotes the undetached retina. **(C)** Higher magnification showing increased retinal thickness (brackets), reduced outer segment length (arrowhead) and ONL disorganization with pyknotic PR nuclei (arrows). Note the subretinal space (red asterisk). **(D-E)** Rat model of retinal detachment. **(D)** Representative fundus photographs and the corresponding OCT images before RD, immediately after RD induction (red asterisk) and 7 days later. RD persists 7 days after induction (red asterisk). **(E)** Retinal semi-thin sections 7 days after RD showing the detached (red box and asterisk) and the undetached areas (black box). Note the increased retinal thickness (brackets) in the detached retina compared to the undetached retina. Furthermore, higher magnification of the detached area showed a loss of the outer segments (arrowhead) and pyknotic photoreceptor nuclei (arrow), as compared with the undetached retina. INL: Inner nuclear layer; IS: Inner segment; ONL: Outer nuclear layer; OS: Outer segment; RPE: retinal pigmented epithelium. Nuclei were stained with toluidine blue. Scale bars: 200 µm (A-E), 500 µm (C; E), 50 µm (B), 25 µm (E, high magnification).

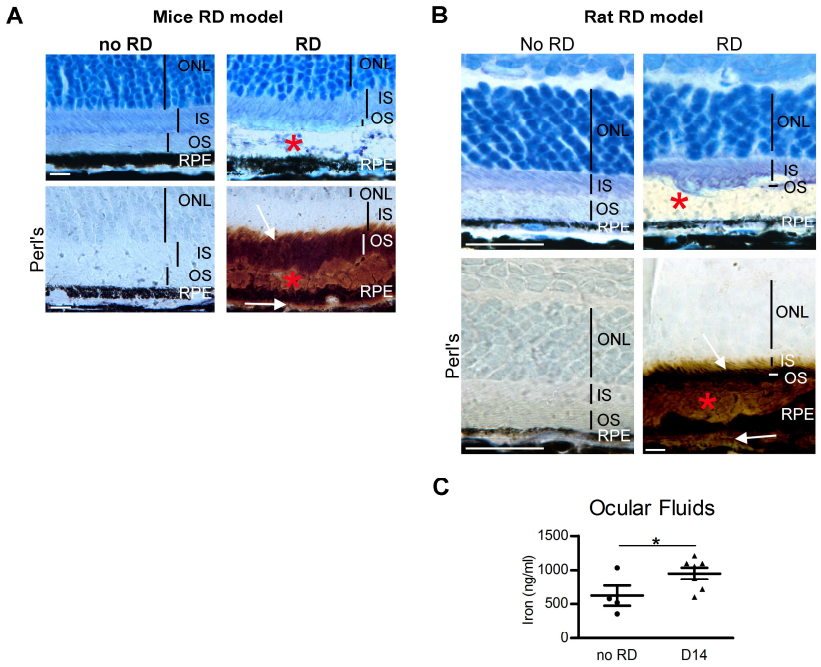

Supplementary Figure 6: Iron accumulates in the rodent retina following retinal detachment.

(A-B) 3,3′-Diaminobenzidine (DAB) amplified Perl's reaction revealed iron accumulation (arrows) in the outer and inner segments and under the RPE layer in mice (A) and rats (B) 7 days after induction of retinal detachment (RD) (red asterisk). **(C)** Iron levels were increased in the ocular fluids of rats 14 days after RD. Mann Whitney test (n=4-6), p=0.042. INL: Inner nuclear layer; IS: Inner segment; ONL: Outer nuclear layer; OS: Outer segment; RPE: retinal pigmented epithelium. Nuclei were stained with toluidine blue. Scale bars: 50 µm (A), 25 µm (B). All values are represented as the mean ± SEM.

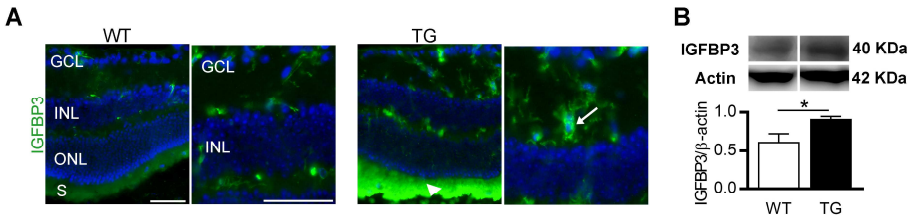

Supplementary Figure 7: The expression of the transferrin protein partner, IGFBP3, in mice following retinal detachment

(A) Insulin-like Growth Factor Binding Protein-3 (IGFBP3) staining was increased in photoreceptor segments (S, arrowhead) and in cells present in the inner plexiform layer (arrow) in retinas from TG mice compared with WT mice, 7 days after retinal detachment induction. **(B)** Western blotting and quantitative analysis of IGFBP3 in the retinas of TG and WT mice 4 days after RD. Mann Whitney test (n=3-5, *p=0.028). GCL: Ganglion cell layer; INL: Inner nuclear layer; IS: Inner segment; ONL: Outer nuclear layer; OS: Outer segment; RPE: Retinal pigmented epithelium. Scale bar: 50 µm. All values are represented as the mean ± SEM.

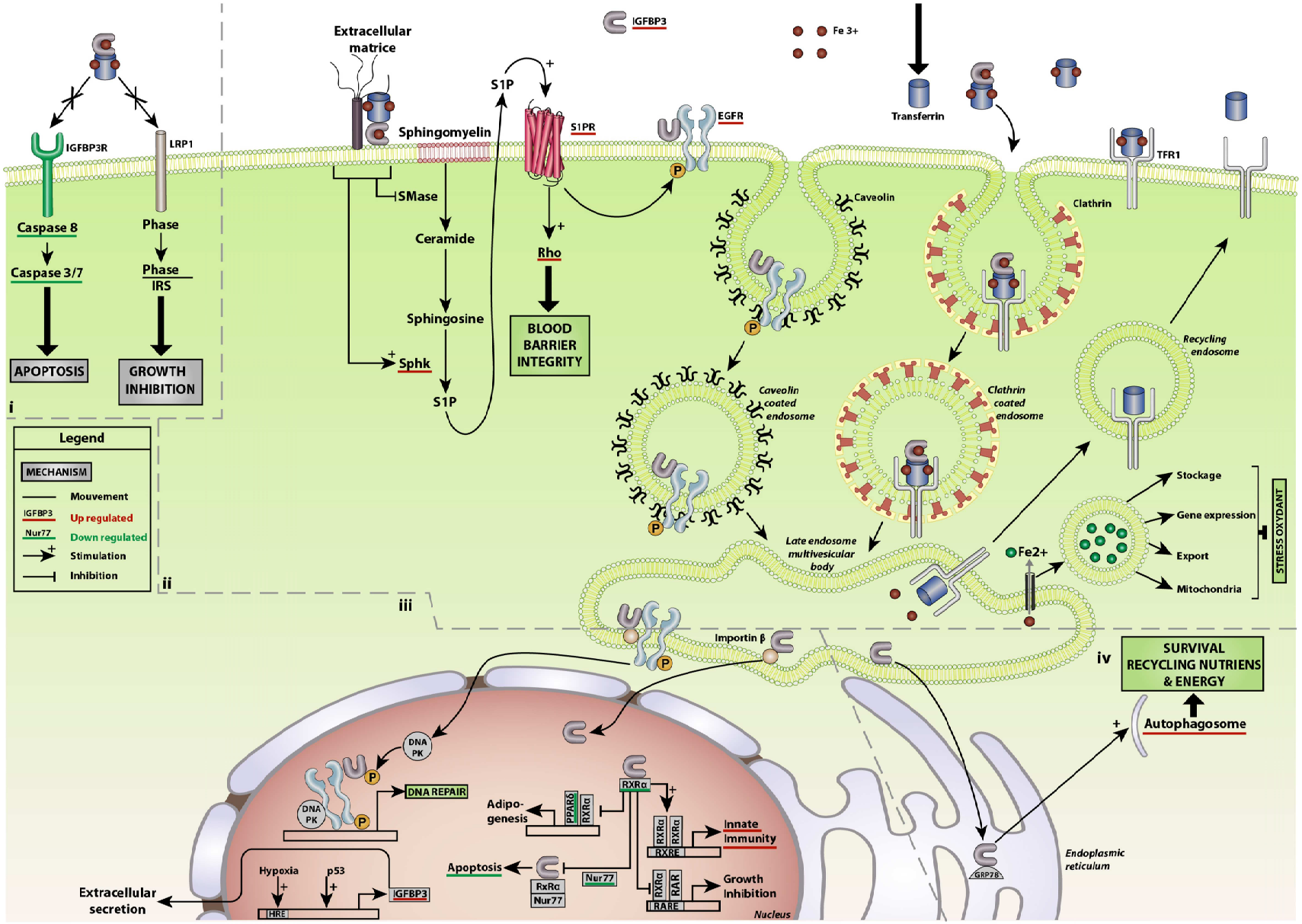
IGFBP3R
LRP1
Caspase 8
Caspase 3/7
APOPTOSIS
Phase
Phase IRS
GROWTH INHIBITION
i
Extracellular matrice
Sphingomyelin
SMase
Ceramide
Sphingosine
Sphk
S1P
S1P
S1PR
Rho
BLOOD BARRIER INTEGRITY
IGFBP3
EGFR
Fe 3+
Transferrin
TFR1
Caveolin
Clathrin
Caveolin coated endosome
Clathrin coated endosome
Recycling endosome
Late endosome multivesicular body
Fe2+
Stockage
Gene expression
Export
Mitochondria
STRESS OXYDANT
ii
iii
Importin β
iv
SURVIVAL RECYCLING NUTRIENS & ENERGY
Autophagosome
DNA PK
DNA REPAIR
Adipo-genesis
PPARδ
RXRα
Innate immunity
RXRE
Apoptosis
RxRα
Nur77
RARE
RAR
Growth Inhibition
Hypoxia
p53
HRE
IGFBP3
Extracellular secretion
Nucleus
GRP78
Endoplasmic reticulum
Legend
MECHANISM
Mouvement
Up regulated
Down regulated
Stimulation
Inhibition

Supplementary Figure 8: Proposed role of IGFBP3 in the protective effect of transferrin

Based on genes up- and down-regulated in transcriptomic analysis, this illustration highlights the cellular protective mechanism involving the IGFBP3-transferrin (TF) interaction. The formation of the IGFBP3–TF complexes may be expected: **i**) to reduce IGFBP3 binding on its cell-surface specific receptors, IGFBP-3R and low-density lipoprotein receptor-related protein-1 (LRP1), and inhibits caspase-dependent apoptosis and growth inhibition through the dephosphorization of the insulin receptor substrate (IRS) by a Ser/Thr-specific protein phosphatase. **ii**) to enhance the interaction of IGFBP3 with multiple extracellular components including glycosaminoglycan (GAG) or receptors for its cellular uptake. IGFBP3 binding to the extracellular matrix promotes sphingosine-1-phosphate (S1P) production by inhibiting sphingomyelinase (SMase) and increasing sphingosine-1-phosphatase (SphK1). S1P interaction with S1PR receptors leads to multi pathways like preservation of blood barrier integrity, and also transactivation of EGFR leading to a caveolin-mediated endocytosis of the complex EGFR-IGFBP3. The IGFBP3-TF complex is taken up by the TF 1 receptor and internalized by a clathrin endocytosis vesicle. IGFBP3 and its binding partners (TF or EGFR) may be then found in the late endosome/multivesicular body for redistribution of molecules in the cell. **iii**) Nuclear import of IGFBP3 is mediated by importin beta, where it can form nuclear complexes. Phosphorylation of nuclear IGFBP3 by DNA-PKcs, resulting in activation of IGBP3-EGFR-DNA-PK complexes and favoring double-strand DNA break repair by non-homologous end-joining (NHEJ). The IGFBP3-RXR alpha interaction increased RXRalpha homodimer transcriptional activity whereas it prevented formation of the RXRalpha-RARalpha, and RXRalpha-PPRAgamma-RXRalpha-Nur77 heterodimers. The endoplasmic reticulum (ER) is one of the probable sources of the autophagosomal double membrane in mammals, and the ER-resident chaperone GPR78 is required for stress-induced autophagy. The interaction IGFBP3 with GPR78 (**iv**) stimulates the autophagic survival response in case of nutrient deprivation or hypoxia. (**for literature review** (*29*, *31*, *32*))

Supplementary Table 1: Top 20 up- and down-regulated genes in TG compared with WT mice following retinal detachment

Gene Symbol	Gene Name	Fold-Change	P-Value	Entrez Gene ID
Genes up-regulated				
Gm19554	predicted gene, 19554	88,67	1,04E-19	100503099
Serpina3h	serine (or cysteine) peptidase inhibitor, clade A, member 3H	22,11	6,88E-05	546546
Snord15a	small nucleolar RNA, C/D box 15A	14,88	3,51E-02	449630
Gab3	growth factor receptor bound protein 2-associated protein 3	4,83	1,14E-02	100503280
Lilrb4a	leukocyte immunoglobulin-like receptor, subfamily B, member 4A	4,48	1,38E-03	14728
Hmox1	heme oxygenase 1	4,28	1,84E-03	15368
Mmp12	matrix metallopeptidase 12	4,27	1,45E-02	17381
Glycam1	glycosylation dependent cell adhesion molecule 1	4,19	3,36E-04	14663
Cym	chymosin	3,87	8,42E-03	229697
Ms4a6d	membrane-spanning 4-domains, subfamily A, member 6D	3,60	1,49E-02	68774
Igfbp3	insulin-like growth factor binding protein 3	3,27	5,28E-05	16009
Fndc1	fibronectin type III domain containing 1	3,20	4,84E-11	68655
Msr1	macrophage scavenger receptor 1	3,00	1,30E-02	20288
Cd36	CD36 antigen	2,85	6,88E-07	12491
Gal	galanin	2,84	1,75E-02	14419
Tmem221	transmembrane protein 221	2,78	1,74E-03	434325
Ccl17	chemokine (C-C motif) ligand 17	2,78	1,06E-02	20295
Sphk1	sphingosine kinase 1	2,75	4,88E-03	20698
Il2rg	interleukin 2 receptor, gamma chain	2,74	4,94E-03	16186
H2-Q7	histocompatibility 2, Q region locus 7	2,74	6,11E-06	15018
Genes down-regulated				
S100a9	S100 calcium binding protein A9 (calgranulin B)	8,34	3,94E-03	20202
G530011O06Rik	RIKEN cDNA G530011O06 gene	6,38	1,03E-02	--
Sik1	salt inducible kinase 1	3,73	9,62E-03	17691

Crnde	colorectal neoplasia differentially expressed (non-protein coding)	3,56	2,33E-05	71296
Thoc2	THO complex 2	3,16	2,79E-04	331401
Klf4	Kruppel-like factor 4 (gut)	3,10	2,39E-03	16600
Zfp26	zinc finger protein 26	2,89	1,80E-03	22688
Klf2	Kruppel-like factor 2 (lung)	2,86	1,65E-03	16598
Tubb2a-ps2	tubulin, beta 2a, pseudogene 2	2,75	3,60E-02	627110
Sec24a	Sec24 related gene family, member A	2,69	5,45E-04	77371
Nipbl	Nipped-B homolog (Drosophila)	2,66	1,19E-02	71175
Tfrc	transferrin receptor	2,50	8,27E-03	22042
Hook1	hook microtubule tethering protein 1	2,48	2,65E-02	77963
Ctif	CBP80/20-dependent translation initiation factor	2,47	1,16E-02	269037
Ncoa2	nuclear receptor coactivator 2	2,46	4,82E-02	17978
Tet3	tet methylcytosine dioxygenase 3	2,44	4,36E-03	194388
Setd7	SET domain containing (lysine methyltransferase) 7	2,32	3,72E-02	73251
Cdon	cell adhesion molecule-related/down-regulated by oncogenes	2,31	6,65E-03	57810
Srgap3	SLIT-ROBO Rho GTPase activating protein 3	2,30	2,38E-02	259302
Rptor	regulatory associated protein of MTOR, complex 1	2,29	1,95E-02	74370

Supplementary Table 2: Pathways and genes regulated by Transferrin and implicated in photoreceptors rescues

Pathways	Genes regulated by TF	Functions	References
Retina homeostasis	*Cdhr1*, *Pcdh15*, *Mak*, *Rp1*, *Ush1g*	found in PR cilium for protein trafficking through the connecting cilium	(*34*)
	Tbc1d14, *Evi5*, *Tbc1d30*, *Usp6nl*	negative regulator of Rab proteins family, implicated in rhodopsin transport in cilium photoreceptors	(*28*)
Immune systems	*Serpina3h*, *Glycam1(7)*, *S100a9, Klf4*, *B2m, Tyrobp, Trem2*	neuroprotective modulation of inflammation	(*40*, *41*)
Phagocytosis	*Cd36*, *Cd14*, *Siglech*	facilitate endocytosis/phagocytosis	(*27*)
	Igfbp3, Sphk, *S1PR*, *PPARg*, *Nur77*, *Rxra*,	intracellular neuroprotective effects of IGFBP3	(*31*) Fig. S8
Neurological process	*Adam17, Lrig2*	regulation of the repulsive guidance molecules	(*37*)
	B2m H2-Q7, *H2-T23*, *H2-K1*	major histocompatibility complex Class I play roles in structural and synaptic remodeling in the developing and mature retina	(*38*)
Mechanism of cell death	*Birc5* (Survivin)	inhibit caspase activation	(*39*)
Metabolism	*Pgf*, *Gal,Calca*	protection for neurons	(*40*, *41*)
	Sik1, *Htr2c, Hcrtr1*	inhibit hyperpolarization of neurons and allow protection	(*42*)
	Dusp1, *Rxra*, *Tek*, K*lf4*, *Igfr2*	inhibit cycle of retinoid that protect PR from light damage	(*43*)

Data files S1: Complete transcriptomic analysis

The file is composed with a list of the regulated genes, the GO analysis and the analysis of splicing factors and others genes encoding for RNA-binding proteins (transcription Factors)